

AN ABSTRACT OF THE THESIS OF

Nicholas M. Boulton for the degree of Master of Science in Radiation Health Physics
presented on March 3, 2017.

Title: Commissioning of the NDDL-40 Neutron Detection System at Oregon State University.

Abstract approved: _____

Steven R. Reese

The Neutron radiography facility (NRF) at Oregon State University (OSU) has been modified to begin working on the non-destructive evaluation of concrete materials to study the early stages of shrinkage, cracking, and water transport of concrete during the curing process.

The objective of this work is to investigate the efficiency and spatial resolution of the NDDL 40 Micro-channel plate (MCP) detector for the use of neutron radiography and tomography with the eventual goal of concrete imaging. Working in collaboration with the School of Civil and Construction Engineering, the NRF at OSU has added a NDDL 40 vacuum sealed neutron imaging detector with a delay line system readout developed by Nova Scientific Inc. The detector

provides leading technology that grants high detector efficiency and high theoretical spatial resolution of $\sim 50\text{ }\mu\text{m}$ which is the major metric for generating both 2D and 3D images. Using the patented technology, the detector uses borated micro-channel plates to convert incoming thermal neutrons through the $^{10}\text{B}(\text{n},\alpha)^7\text{Li}$ process. This converts the neutron into an α and lithium ion, which through secondary interaction create an electron avalanche and is amplified to a signal that can be detected.

The NDDL 40 MCP detector has been shown to be capable of producing radiographs and tomography. Through tedious procedures radiographs continually had inconsistent results in image quality due to the dynamic background, signal to noise ratio and dramatically decreased detector efficiency. This led to issues in the rendered tomographic models. Through the extensive measurements and the use of ASTM standards the NDDL-40 MCP detector was determined to have an optimum efficiency of 6% with a maximum spatial resolution of 50 to $200\text{ }\mu\text{m}$.

©Copyright by Nicholas M. Boulton

March 3, 2017

All Rights Reserved

Commissioning of the NDDL-40 Neutron Detection System at Oregon State University

by

Nicholas M. Boulton

A THESIS

submitted to

Oregon State University

in partial fulfillment of

the requirements for the

degree of

Master of Science

Presented March 3, 2017

Commencement June 2017

Master of Science thesis of Nicholas M. Boulton presented on March 3, 2017

APPROVED:

Major Professor, representing Radiation Health Physics

Head of the School of Nuclear Sciences and Engineering

Dean of the Graduate School

I understand that my thesis will become part of the permanent collection of Oregon State University libraries. My signature below authorizes release of my thesis to any reader upon request.

Nicholas M. Boulton, Author

ACKNOWLEDGEMENTS

I would like to my thank family and friends for the support. I would like to give a special thanks to Dr. Steve Reese for the guidance and support. I would like to also thank Dr. Jason Weiss for funding my Graduate Research Assistantship at Oregon State University.

TABLE OF CONTENTS

Introduction	1
1 Literature Review	2
1.1 History	2
1.2 Neutron Sources	3
1.3 Instrumentation	5
1.4 Neutron Radiography Methods.....	7
1.4.1 Direct Radiographic Method	7
1.4.2 Indirect Radiographic Method	7
1.4.3 Electronic Imaging Method.....	7
1.5 Tomography	8
2 Materials and Methods	12
2.1 The Reactor.....	12
2.2 Gold Foil Experiment.....	14
2.3 Detector.....	18
2.3.1 Micro Channel Plates.....	18
2.3.2 Anode.....	20
2.3.3 Electronic Configuration	23

2.4	Standards	24
2.5	Cadmium Strip.....	29
2.6	Beam Evaluation Throughout a Day	30
2.7	Reactor Power Evaluation	31
2.8	Radiography Reconstruction	32
2.9	Tomography Reconstruction	34
2.10	Concrete Samples	40
3	Results and Discussion	43
3.1	Gold Foil Experiment	43
3.2	Detector Efficiency	44
3.3	Standards	44
3.4	Cadmium Strip.....	45
3.5	Beam Evaluation Throughout a Day	46
3.6	Reactor Power Evaluation	48
3.7	Tomography	50
3.8	Complications.....	54
4	Conclusion	58
5	Future Work	59
	Bibliography.....	60

LIST OF FIGURES

Figure 1 Attenuation Coefficients of Neutrons and X-Rays [5]	6
Figure 2 Top view of OSU TRIGA Mk II research reactor.	13
Figure 3 Collimator cross section	14
Figure 4 The gold foils used for Thermal Neutron Flux Determination.....	16
Figure 5 The bare gold foil (left) and gold foil in the Cd cover (right) positioned in front of the beam.	16
Figure 6 Decay Scheme of Au 198 to Hg 198. [23].....	17
Figure 7 Cutaway view of MCP glass plate. [25]	19
Figure 8 Diagram of $^{10}\text{B}(\text{n},\alpha)\text{Li}^7$ [12]	19
Figure 9 Schematic of neutron detection within micro-channel plate [12].....	20
Figure 10 View of the Cross-delay line anode that is set behind the MCPs.	21
Figure 11 Layout of MCP and Anodes [26].....	22
Figure 30 Image of lab setup with High Voltage Power Supply and Quad-Channel USB 2.0 Time to digital converter.	24
Figure 11 Schematic of Beam Purity Indicator.	25

Figure 12 Sensitivity Indicator Schematic [27]	26
Figure 13 Sensitivity Indicator [28]	28
Figure 14 Schematic of Cadmium strip in inches	30
Figure 15 Various images and results of post imaging processing.	34
Figure 18 Detector setup with BPI.....	35
Figure 19 Overall set up for tomography of BPI including linear and rotational stages.	36
Figure 20 Motion controller used for motorized stages	37
Figure 21 four-pixel example of the ART algorithm [30]	39
Figure 22 Images of Entrained Air Cement based mortar samples: (Top Left) M3 Dry, (Top Right) M3 Saturated, (Bottom Left) M6 Dry, (Bottom Right) M6 Saturated.....	41
Figure 23 BPI (left) and SI (right) used for beam quality evaluation.	45
Figure 24 Image of Cadmium Strip with various tolerances.	46
Figure 25 Graph of coincidence vs detector voltage at various reactor power levels.....	50
Figure 26 BPI and represented Sinograms.....	51
Figure 27 Front View of BPI Tomographic image	52
Figure 28 Side View of BPI Tomographic Image	53

Figure 29 Isomeric view of BPI Tomographic image.....	53
Figure 30 Top view of BPI Tomographic Image	54
Figure 31 Image of cadmium strip at 100% reactor power.....	55
Figure 32 Example of an image taken with dual exposure.	56
Figure 33 BPI image with electronic noise	57

LIST OF TABLES

Table 1 Neutron Energy ranges.....	5
Table 2 Quantitative definitions of Beam Purity Indicator.	25
Table 3 Neutron Radiography standards.....	27
Table 4 Determination of H	28
Table 5 Determination of G	29
Table 6 Measurements used for Gold foil experiment.....	43
Table 7 International ASTM E545 suggested values for NDDL 40 Detector	45
Table 8 Initial Measurements prior to test of measure the change in flux and exposure over a MW day.....	47
Table 9 Results of Flux determination and gamma exposure	47
Table 10 Measurements after shutdown.	47
Table 11 Results of measured counts at various voltages through different reactor power levels.	48
Table 12 The second set of measurements taken at 10% power.....	50

Introduction

The Neutron radiography facility (NRF) at Oregon State University (OSU) has been modified to begin working on the non-destructive evaluation of concrete materials to study the early stages of shrinkage, cracking, and water transport of concrete during the curing process.

The objective of work is to optimized efficiency and spatial resolution of the NDDL 40 Micro-channel plate (MCP) detector for the use of neutron radiography and tomography with the eventual goal of concrete imaging. Working in collaboration with the School Civil and Construction Engineering, the NRF at OSU has added a NDDL 40 vacuum sealed neutron imaging detector with delay line readout developed by Nova Scientific Inc. The detector provides leading technology that grants high detector efficiency and high theoretical spatial resolution of $\sim 50 \mu\text{m}$ which is the major metric for generating both 2D and 3D images. Using the patent technology, the detector uses borated micro-channel plates to capture the incoming thermal neutron using the $^{10}\text{B}(\text{n},\alpha)^7\text{Li}$ process. This converts the neutron into an α and lithium ion, which through secondary interaction creates an electron avalanche and is amplified to a signal that can be detected.

Through the process of measurements and methods of determination, ASTM standards were applied to evaluate 2D projections. The detector efficiency and spatial resolution were established from these images and tests to determine the capability of the NOVA Scientific NDDL40 detector.

1 Literature Review

1.1 History

Neutron Radiography is a nondestructive method used to examine the interior portion of objects that are opaque to visible light. It is used to produce two-dimensional images by transmitting neutrons through the object and on to a neutron sensitive detector or film. Initial radiography was performed with X-rays for many applications including imaging the human body for medical diagnosis and therapy[1].

X-ray radiography has also been extensively used for nondestructive testing for quality control. For instance, the applications of X-ray radiography may include the imaging of welds along pipe lines, inspection for foreign objects in consumer good, and the inspecting of fatigue in components for ships and aircrafts. [1]

The neutron was postulated by Rutherford in the 1900's but was first discovered in 1932 By James Chadwick. Kallmann and Kuhn produced the first image using neutrons in 1935 [2]. Their experiment used a neutron generator with a weak neutron beam so the image was not of useful contrast. The exposure thus required too many hours to perform and led to the reluctance of further exploration of research in neutron radiography.

Along the same time as Kallmann and Kuhn were evaluating neutrons for radiography, a study was being conducted by Peter [1]. With an order of magnitude high beam intensity, Peter achieved better image quality. This was due to his

accessibility to a neutron generator capable of producing a flux with a magnitude greater than that of what Kallmann and Kuhn were using. The high beam intensity allowed him to take radiographs in minutes instead of hours [1]. The development of neutron radiography stopped until after WWII. By the 1970's, many research reactors with in the United States and Europe had facilities capable of performing neutron radiography of useful quality [3]. For further development in neutron radiography, meetings were held internationally to promote collaboration among peers. The first topical meeting specifically on neutron radiography was held in Birmingham, England in 1973. By 1979 a committee was formed called, "The Neutron Radiography Working Group." The Groups' first conference was held in Denmark with a following conference in 1986 in Paris, France [4].

1.2 Neutron Sources

There are several methods to produce neutron beams with sufficiently high intensity. Examples include a neutron generator, radioisotope sources, and nuclear reactor. Each neutron source can provide a flux adequate for neutron radiography. A neutron flux is a term used to describe the number of neutrons traveling across a unit area in a unit time.

An accelerator source is a device that produces neutrons by bombarding a metal or material with deuterons or protons. The products of these reactions result in a neutron and a recoil daughter particle. Some typical reactions are $^9\text{Be}(d,n)^{10}\text{Be}$, $^3\text{H}(d,n)^4\text{He}$, $^2\text{H}(d,n)^3\text{He}$, and $^2\text{H}(p,n)^3\text{He}$. The most commonly used reactions

involve the $^3\text{H}(\text{d},\text{n})^4\text{He}$ and $^2\text{H}(\text{d},\text{n})^3\text{He}$, called d-T and d-d reactions, respectively. The result of such interactions is either a 14.1 MeV or 2.5 MeV neutron energy, respectively [1].

Another common source of neutrons is a radioactive source that undergoes spontaneous fission. Unlike the accelerator method for producing neutrons, this method relies on the production of neutrons directly and indirectly from the decay of the isotope. A common example of this is Californium-252. This is an isotope with a relatively short half-life of 2.6 yrs which decays through either spontaneous fission or alpha decay. One milligram of Cf-252 can emit neutrons at a rate of 2.3×10^9 dps. These types of sources are for use in small, portable devices.

The best method for producing large number of neutrons involves using a nuclear reactor. A nuclear reactor is a device designed to control and sustain a nuclear chain reaction. Many of these reactors can be differentiated by the design defined by the type of moderator, coolant and fuel. Generally though, they are differentiated into two categories, research reactors and power reactors. Research reactors tend to be operated by universities or labs while power reactors, larger in scale, are used to generate electricity. Research reactors can start up and shut down numerous times during a lifetime of the fuel burnup while a power reactor usually have a continuous operating tempo.

For all types of sources, consideration needs to be made for collimating, moderating, shielding and/or geometry alteration to eliminate gamma rays,

moderate fast neutrons to produce a beam containing a uniform thermal neutron flux. These considerations are important to take in account when considering the energy range of neutrons that are desired. A neutron can be generally categorized based on its energy: fast, epithermal, and thermal as shown in Table 1. For radiography purposes, a neutron beam is usually thermalized so that most of the neutron population lies in the thermal energy range.

Table 1 Neutron energy ranges

Neutrons	Energy Range
Thermal	0.025 eV
Epithermal	0.025 – 0.4 eV
Fast	1 – 20 MeV

1.3 Instrumentation

There are many different techniques for performing radiography, each providing different information. X-ray radiography was already well established before neutron radiography.

The difference between X-rays and neutrons is seen in their absorption coefficients. For X-rays, as an atom increases in size, or atomic number, the absorption coefficient increases. Due to the increase of absorption with respect to atomic number, it is impractical to perform X-ray radiography with materials that contain compounds of higher atomic numbers and density.

Neutrons are only effectively attenuated by a few isotopes. These include isotopes of, hydrogen, boron, cadmium, gadolinium, and samarium. The relationship between X-ray and neutron attenuation by element can be seen in Figure 1.

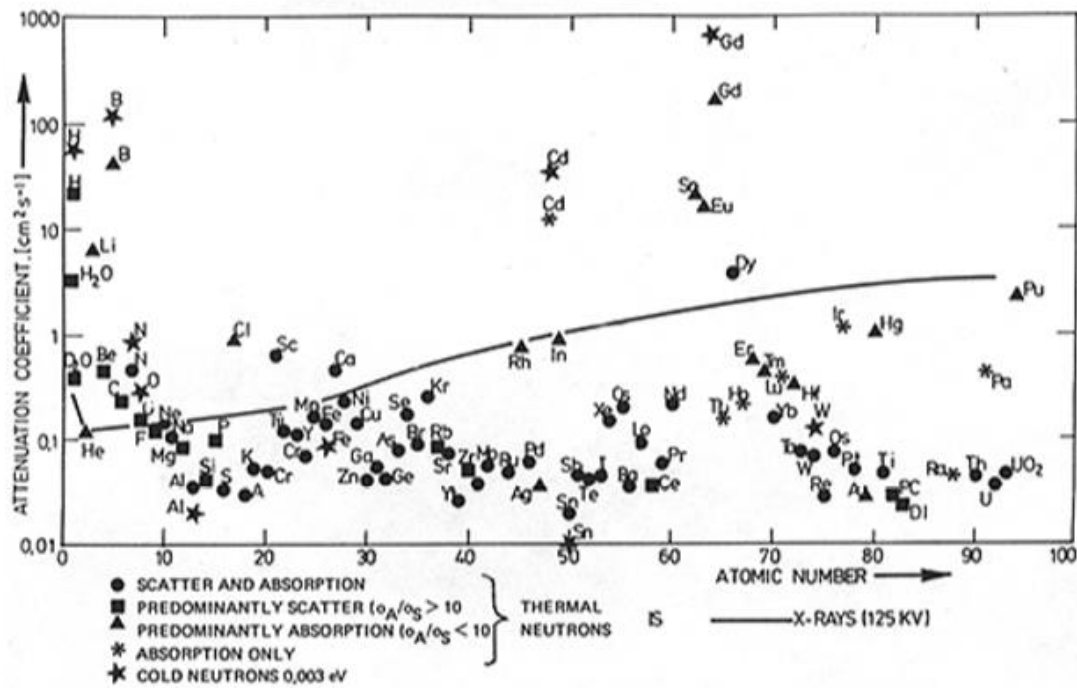


Figure 1 Attenuation Coefficients of Neutrons and X-Rays [5]

From Figure 1, the attenuations coefficients for neutrons do not follow a log linear trend line like X-rays attenuation coefficients. Neutrons seem to follow a random trend when compared with increasing atomic number.

Because neutrons interact directly with the nucleus of an atom, a detector must consist of a material that can effectively attenuate neutrons. Due to the

difficulty of this, most detectors use materials to convert neutrons in to other particles that can be recorded easier.

1.4 Neutron Radiography Methods

1.4.1 Direct Radiographic Method

For x-rays, a film is used to convert the incoming particle to light. Unfortunately, photographic film cannot attenuate neutrons. Due to this problem, a converter is placed in front of the photographic film. An example of this would be a radiograph using film with gadolinium foil, the converter, placed over of the photo-sensitive film. As the gadolinium foil absorbs neutrons, it undergoes internal conversion, emitting low energy electrons. [6]

1.4.2 Indirect Radiographic Method

The indirect radiographic method describes an imaging technique where the image recorder is not in direct contact with a converter screen. This method is also called transfer exposure. For this method, a metal foil, usually containing dysprosium or indium, is exposed to a neutron beam then placed upon the photo-sensitive film post irradiation. The photographic film produces a radiograph by capturing the beta particle released from the decay of dysprosium or indium. [5] [6] Both the direct and indirect methods can have resolution on the order of tens of microns [5]. However, both methods have long production time intervals making them not optimal for tomography.

1.4.3 Electronic Imaging Method

There are methods that do not require film to produce an image from neutron radiography. Recording images can be achieved using a digital electronic device. This is done by using a detection system and recorder in connection with a charged-coupe device (CCD) camera. The electronic imaging usually utilizes scintillation detectors. An example

of this was used at the National Institute of Standards and Technology (NIST) Center for Neutron Research in 2005 to perform dynamical studies of proton exchange membrane fuel cells. NIST used a converter screen coupled to a scintillator, a mirror, a condensing lens and a CCD camera. The system works by reflecting the scintillation light (generated by the converter electron interaction with the scintillator) with the mirror to the CCD camera. NIST's detection setup allows for quick acquisition of images but was only able to acquire a spatial resolution of about 200 μm . The quick acquisition is optimal for tomography by minimizing time to perform work and fewer radiographs required to be taken [7].

In the past, these types of systems utilized video cassette recording to record the images. Today's technology allows the transfer of data directly to a computer for the ease of image editing and processing. The electronic method has a small decrease in spatial resolution when compared to the radiographic film. But the reduced image production time makes tomography viable.

The Solid State Physics Division (SSPD) of Bhabha Atomic Research Centre (BARC) has also been conducting its own research in the development of neutron detection and radiography. BARC is focused on the design and development of neutron detectors and neutron radiography using a 400 kW pool type reactor. SSPD used a scintillator screen made of $^6\text{LiF}+\text{ZnS}$ and a CCD camera. The facility was able to produce radiographs with a spatial resolution of $\sim 300 \mu\text{m}$ with success in producing tomographic images. [8]

1.5 Tomography

Tomography is a radiography method first developed for medical X-ray radiography in which a series of images are taken at various positions around the target, and by use of computer software for image processing, the radiographs are transposed to give an image of cross sections at 90 degrees to the image. [5]

The first computed tomographic (CT) image was created in London by Godfrey Hounsfield in 1971. Hounsfield theorized that one could see into an object if X-rays were taken from different angles of the object by putting each image together to form an 3D model normal to an axis. Hounsfield formed the first axial tomography machine which is known today as the CT machine. [9]

Many early efforts demonstrated the possibilities but were prevented by the ability to produce an adequate neutron flux, the lack of high resolution digital sensors, and poor computing capabilities with minimal memory space. [10].

In 2006, NOVA scientific developed a neutron sensitive MCP detector for improving neutron radiography. The spatial resolution was comparable if not better than modern systems to date, but the detector efficiency was found to be approximately 18-21%. [11] [12]

The MCP's in NOVA's detector consisted of a proximally 1 mm thick glass disks that were constructed with microscopic parallel channels running through them. Thorough research has been performed on these MCPs at the University of California at Berkeley. Though the detector efficiency hasn't been determined for one MCP, calculations proposed that stacks of MCPs will be able to yield a detector efficiency of 78%. [11] [12]

In 2013 at Oregon State University, a similar study was done by Williams with a MCP detector from Nova Scientific with the task of determining and optimizing the resolution for neutron radiography and tomography [11]. Extensive research was performed to optimize the detector system with a single MCP. Results showed resolution of radiography and tomography of the MCP detector to be close to 25 μm . [11]

Williams found that various corrections and measurements with respect to the dynamic background were required to get to the maximum spatial resolution. It is typical for a tomography procedure to collect images and normalize with the a set of background images. However, with this detector setup it was found to not be possible. The dynamic background relative to the detector was found to create too much difficulty in obtaining appropriate contrast in final radiographs.

Though the work by Williams found the detector to be capable of producing radiographs and tomographic images, inconsistencies in radiographs and the detector made the setup difficult to use. This was related to the fact the dynamic background forced the operator to collect twice as many images to construct tomography.

A study in 2014 at the European Council for Nuclear Research (CERN) further investigated micro-channel plates and vacuum detectors. The study specifically studied the new manufacturing processes that result in significant improvement in terms of efficiency, noise, and lifetime performance [13]. The study discussed the developments of MCP photomultiplier tubes (PMT). Due to the intrinsic properties, MCP-PMTs are appropriate detectors for applications involving strong magnetic fields. The study discovered that if the MCP-PMT axis was aligned with the magnetic field that there was an improvement with spatial resolution and but effects from backscatter remained an issue. [14] [13].

T. Gys further investigated a study by Barnyakov and Mironov dealing with the aging of the photocathode in MCP-PMT. Barnyakov and Mironov showed that performance degradation was essentially due to the ion feedback effects that affecting the photocathode and time resolution. Development in improved MCP scrubbing and treated bialkali photocathodes increased multiplier gain and showed an increased robustness in ion feedback up to a few C/cm^2 . [15] [13].

Technology surrounding the MCP design is continuously evolving and improving. With research focused on increasing MCP lifetime and more reliable anode segmentation will result in higher individual channel counts. This consequently results in a required high speed and high signal to noise ratio that will represent a challenge for the future research.[13]

2 Materials and Methods

2.1 The Reactor

The Radiation Center at OSU has a TRIGA Mk II research reactor. It is a water cooled, pool-type reactor designed to operate at a steady state of 1MW. The core is placed at the bottom of a 22' deep concrete pool with concrete walls acting as structural support and shielding for the reactor bay. The reactor was designed with three radials and one tangential beam port. [16]

Shown in Figure 2, beam port 3 is tangentially located to the reactor core. Built within beam port 3 is a convergent/divergent collimator. The collimator is designed to deliver a high uniform thermal flux while minimizing the gamma rays from the reactor. As shown in *Figure 3* the collimator was built with a series of boral, cadmium, and lead discs.

The beginning of the collimator contains a bismuth filter. This high Z filter is placed to reduce gamma rays; however, it also has a relatively small neutron absorption and scatter cross section. Following the column down to the end of the convergent section, the column comes to a boral, cadmium, and polyethylene aperture. This section of the collimator provides uniformity to the beam. At the end of the collimator is a boral plate with a rectangle opening used to remove thermal neutrons from the useable section of the beam reducing umbra and penumbra. Measurements indicated that the beam met requirements of ASTM E545, Category 1 neutron radiography beam. [17]

In 2005, NRAY Services INC. performed a beam port evaluation of the collimator in beam port 3 to determine the length over aperture diameter ratio (L/D). To date, many neutron radiography facilities use a similar geometry where the collimator is described by the diameter, D , of a small aperture close to the source and the length, L , of the distance between the small aperture and sample position. For neutron radiography, the L/D ratio is a way to characterize the performance of a component or facility [18]. NRAY used a no umbra device based on ATSM E803, *The Standard Test Method for Determining L/D ratio of Neutron Radiograph beams*. The test measures the effective collimation ratio, L/D , of the beam. The evaluation by NRAY determined the L/D ratio of the collimator was 100:1 at 6 ft from end of the beam port [19].

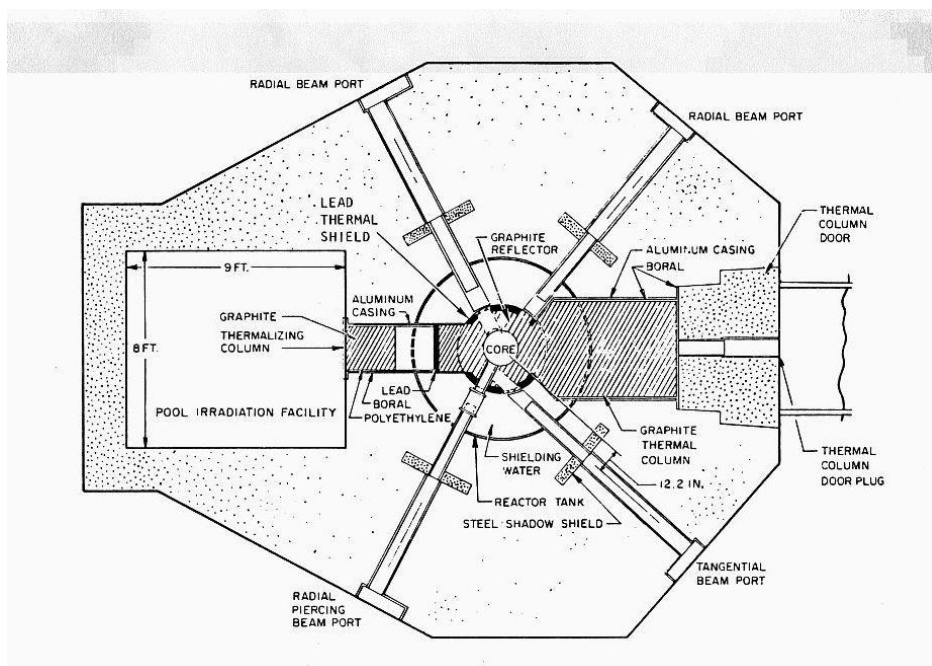


Figure 2 Top view of OSU TRIGA Mk II research reactor.

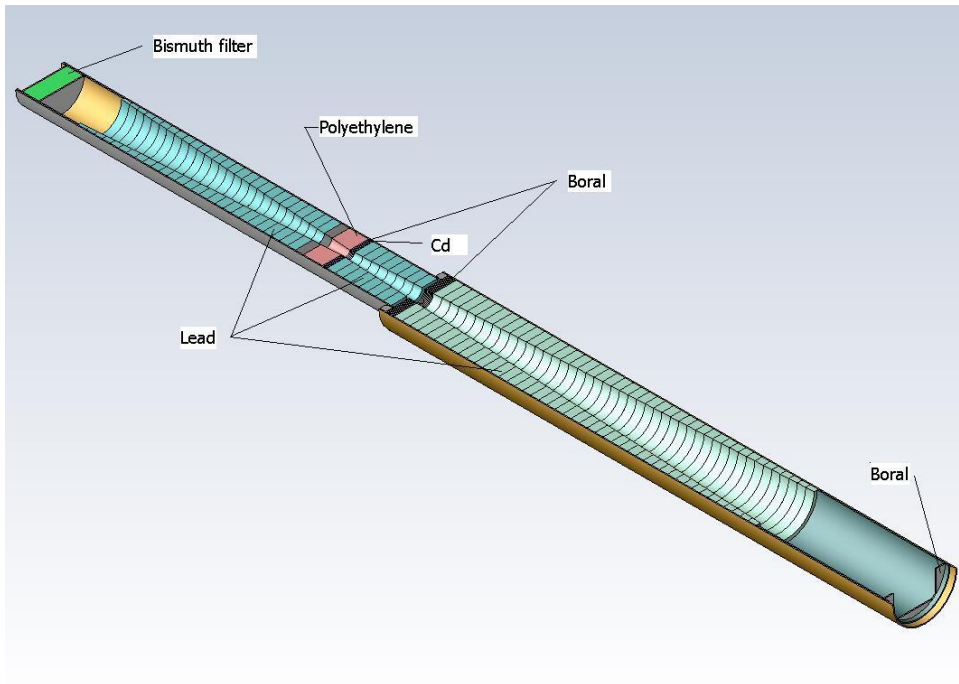


Figure 3 Collimator cross section

2.2 Gold Foil Experiment

Before determining the detector efficiency, the thermal neutron flux needed to be measured. This was performed by placing gold foils within the neutron beam. Activation was used to produce secondary particles which are proportional to the neutron flux and are easier to detect. The sample is activated and decays concurrently and by knowing these two competing processes the activity can be determined at any point in time, using the following differential equations:

$$\frac{dN}{dt} = R - \lambda N \quad (1)$$

where dN/dt , the rate of change in radioactive nuclei overtime, is found to be the difference between the rate of activation, R , and the decay, λN , which is the product of the decay constant, λ , and the number of radioactive nuclei, N .

Integration the of equation yields,

$$N(t) = \frac{R}{\lambda(1 - e^{-\lambda t})} \quad (2)$$

multiplying each side by λ ,

$$A(t) = N(t)\lambda = R(1 - e^{-\lambda t_0}) \quad (3)$$

yields an equation for the activity at a point in time.

After an irradiation of 7 hours at 1 MW from the TRIGA reactor, the radioactivity on each of the two foils was measured using a HPGe detector. Because the foils are continually decaying after irradiation, the time between each step must be accounted for; through the following equation [20]:

$$A = \frac{\lambda(C - B)}{\varepsilon(1 - e^{-\lambda t_0})(e^{-\lambda t_1} - e^{-\lambda t_2})} \quad (4)$$

where C , the counts measured from the detector, B , the number of background counts expected in the counting time, t_0 , the time of irradiation, t_1 , the time of the foils removal from the neutron flux, t_2 , the time the foils are counted by the HPGe detector, and ε , the overall counting efficiency of the detector.

The foils used for the flux measurement are shown Figure 4. Each gold foil was of the same purity, size and thickness. For the measurement, one bare foil was placed in front of the beam while the other foil was placed in a Cd cover in the beam. The difference in radioactivity between the two foils can be used to determine the flux from thermal and epithermal/fast neutrons.



Figure 4 The gold foils used for Thermal Neutron Flux Determination



Figure 5 The bare gold foil (left) and gold foil in the Cd cover (right) positioned in front of the beam.

The idea behind the Cd cover is that the thermal neutron cross section in Cd is very large but dramatically reduces at about 0.5 eV. Therefore the gold behind the Cd cover is

activated by fast and epithermal neutrons only. The small epithermal and fast neutron flux is in part due to the geometry of the beam port with respect to the core which helps limit the amount of epithermal and fast neutrons travel down the port. By subtracting the amount of activation of the Cd covered gold foil from the uncovered gold foil, shown in equation 5, the activity due to thermal neutrons was calculated.

$$A_{th} = A_{tot} - A_{ep,f} = \frac{\text{neutron}}{s * cm^2} \quad (5)$$

Au-197, has a thermal cross section of 98.65 barns [21]. After activation, it becomes Au-198 which has a half-life, $T_{1/2}$, of 2.7 days. In 99.98% of the time, Au-198, decays with beta emission to an excited state of mercury. In approximately 96% of the time, the excited mercury atom emits a 411 keV gamma ray [22]. The decays scheme of the activation is shown in Figure 6.

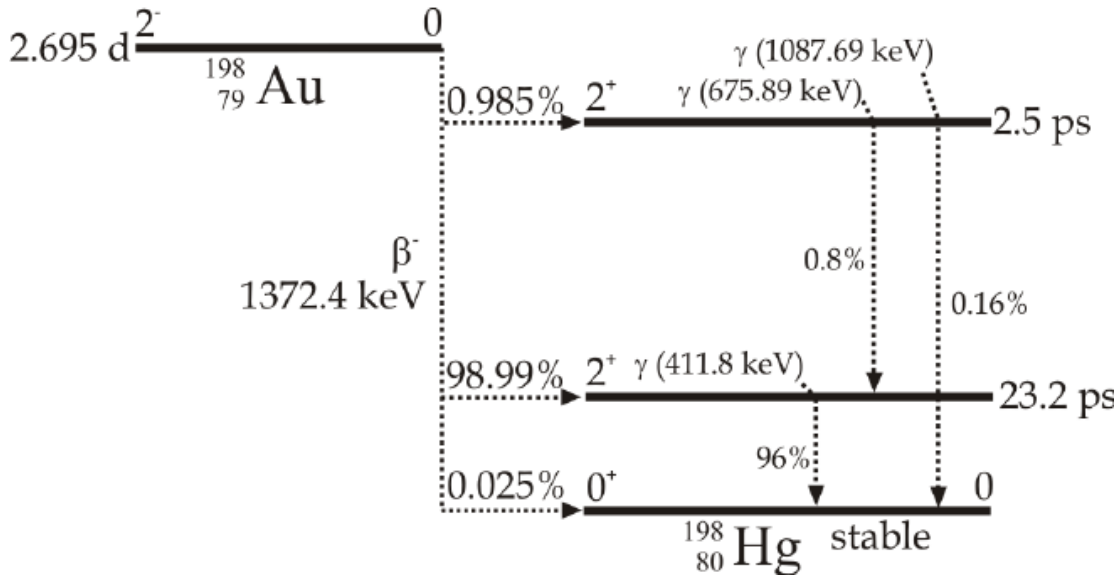


Figure 6 Decay Scheme of Au 198 to Hg 198. [23]

The absolute thermal neutron flux was obtained from the activities measured of the bare and Cd covered foils after applying foil weight, foil density, cooling time and irradiation time corrections, as shown below;

$$A = (\phi_{th}\sigma_{th} + \phi_{epi}\sigma_{epi}) * N(1 - e^{-\lambda t}) \quad (6)$$

Solving for ϕ_{th} ,

$$\phi_{th} = \left(\frac{A_{Au}}{N_{Au}(1 - e^{-\lambda t})} - (\phi_{epi} * \sigma_{epi}) \right) / \left(\sqrt{\frac{\pi}{2}} * \sigma_{th} \right) \quad (7)$$

2.3 Detector

The NDDL 40 MCP detector was purchased from Nova Scientific in Spring 2016 by Oregon State University. The sealed detector contains two neutron sensitive micro-channel plates with a delay line anode output. The detector allows for high spatial and temporal resolution.

2.3.1 Micro Channel Plates

Shown in Figure 7, MCP's are 1mm thick glass plates with millions of channels through each plate. Each channel running in parallel of 4 to 100 μm in diameter with the center line to center line of each channel being $\sim 10 \mu\text{m}$ [24].

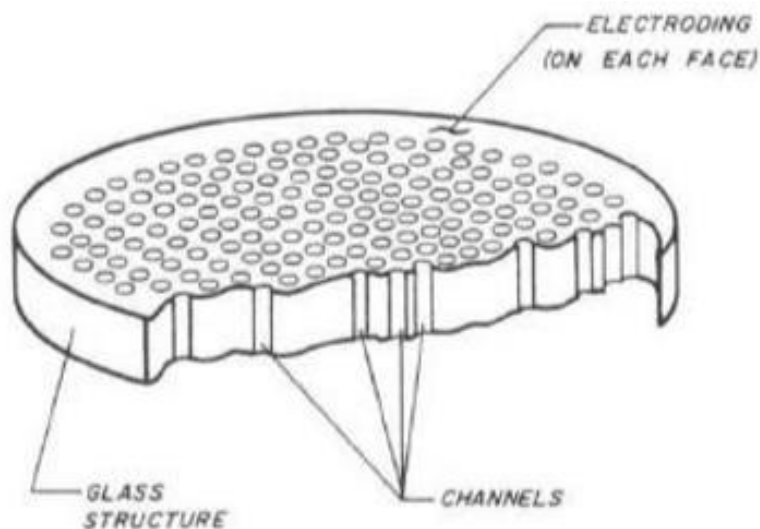


Figure 7 Cutaway view of MCP glass plate. [25]

These micro-channel plates are doped with boron, because of its large thermal neutron cross section. As the neutron comes in, it interacts with the walls of a channel. This interaction produces a $^{10}\text{B}(n,\alpha)\text{Li}^7$ reaction described in Figure 8.

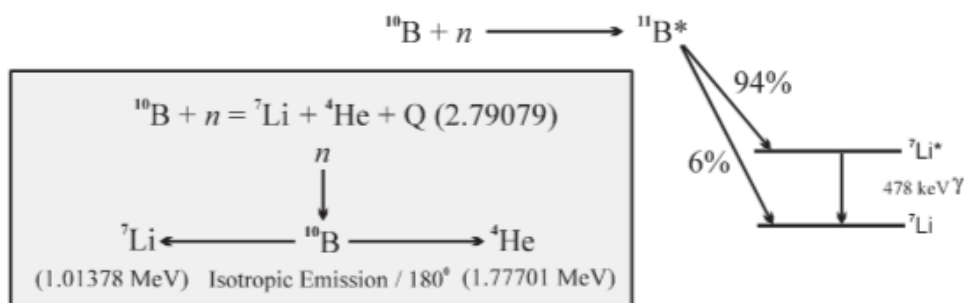


Figure 8 Diagram of $^{10}\text{B}(n,\alpha)\text{Li}^7$ [12]

The recoil alpha particle interacts with the wall creating secondary electron interactions. As the interactions occur down the channel the secondary electrons create an electron avalanche. This creates an outward pulse from the anode which is registered by the detector as a count [24].

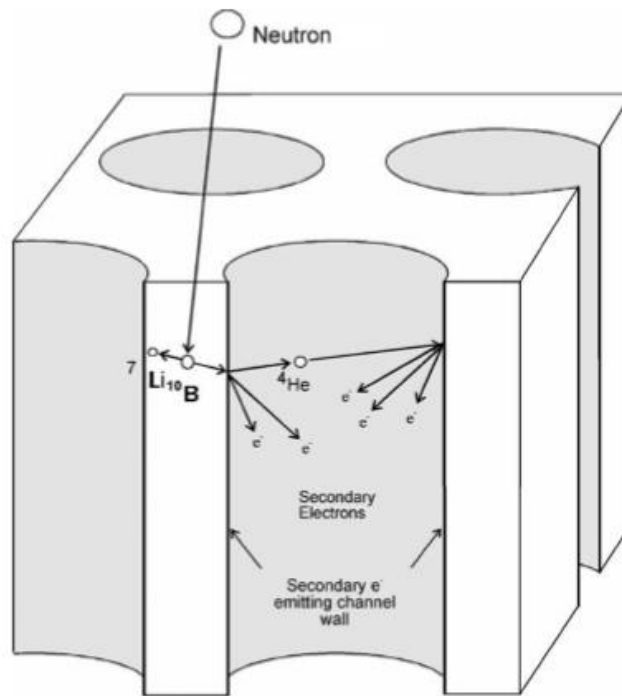


Figure 9 Schematic of neutron detection within micro-channel plate [12]

The initial neutron interaction with the MCP tends to be towards the front of the MCP stack due to the high cross section. In the end, this geometry produces a gain of 10^6 to 10^7 [11].

2.3.2 Anode

As the electrons cascade through the MCPs, they are drawn to the anode by a positive potential difference between the anode and the backside of the MCP stack. This setup can be shown in Figure 10. The electron cloud saturates a cross delay line where the electrons induce an electrical pulse in to the delay line by capacitive coupling. An illustration of this phenomenon is shown in Figure 11. The cross-delay line anode layout allows the software to interpret the charge resulting in an output of an event location with a spatial resolution of $10\ \mu\text{m}$ [12]. With a short travel interaction length of $3.5\ \mu\text{m}$ in

any direction from the alpha particle, the theoretical maximum neutron spatial resolution for the interaction is about $17\text{ }\mu\text{m}$. [12]



Figure 10 View of the Cross-delay line anode that is set behind the MCPs.

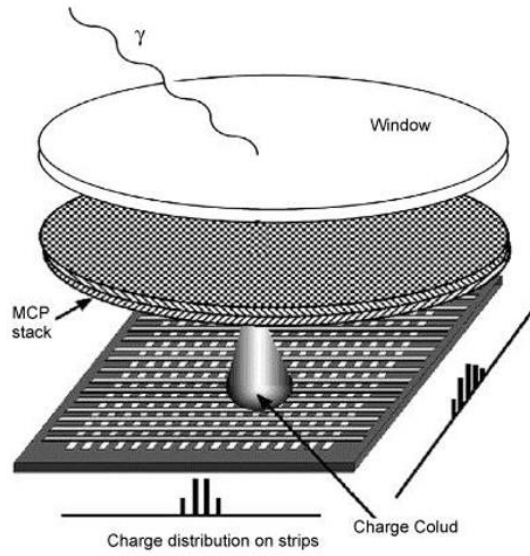


Figure 11 Layout of MCP and Anodes [26]

For a boron doped MCP detector, the neutron detection efficiency, Q_n , is the product of three terms.

$$Q_n = P1 * P2 * P3 \quad (8)$$

where P1 is the fraction of incident neutrons absorbed, P2, the fractions of incident neutrons absorbed to produce an electron avalanche, and P3, the fraction of avalanches registered by the electronics. In other words, P3 is the fraction of interactions that lead to a successful electron avalanche to the anode. An assumption is made that $P3=1$ because once an electron avalanche is created, it will always yield a detectable pulse to the anode. This assumption was proven true through the research previously done by Tremsin. [12]

2.3.3 Electronic Configuration

The high voltage power supply of the detector has a significant contribution to the resolution of every radiograph. From the main power supply, the user can increase potential in increments of 1, 10, 100, and 1000 volts to a desired voltage. It was found that the minimum voltage the detector will begin gather significant counts was 3400 volts. From there, the voltage was increased in increments of 50 V until the count rate was optimized. An optimum voltage was found at 3850 V. Unlike previous models of the MCP detector from NOVA Scientific, the threshold and timing within the preamplifier, the fraction discriminator, and time delay card are built into one unit. NOVA has come up with algorithms to optimize all timing and thresholds required for color gradient, count registration, and noise from the oscilloscope. The high voltage power supply and accompanied electronics are shown in Figure 12.



Figure 12 Image of lab setup with High Voltage Power Supply and Quad-Channel USB 2.0 Time to digital converter.

2.4 Standards

ATSM E545, describes a method for determining image quality of a thermal neutron beam that is specifically used for radiography. The standard describes the use two different objects part of the Image Quality Indicator (IQI) system.

The first IQI used is called the Beam Purity Indicator (BPI). This object is constructed as a polytetrafluoroethylene block containing two boron nitride disks, two lead disks, and two cadmium strips. This quantitative test that provides a method for determining the thermal neutron content, gamma content image sharpness, and overall quality. A schematic of the BPI is shown in Figure 13 with quantitative definitions listed in Table 2.

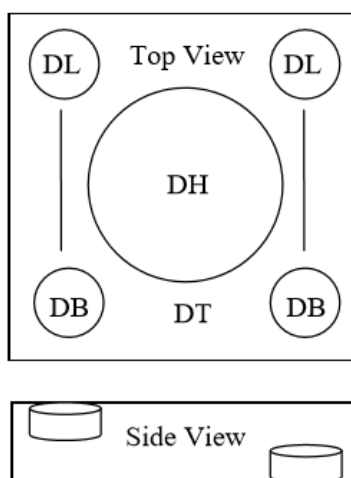
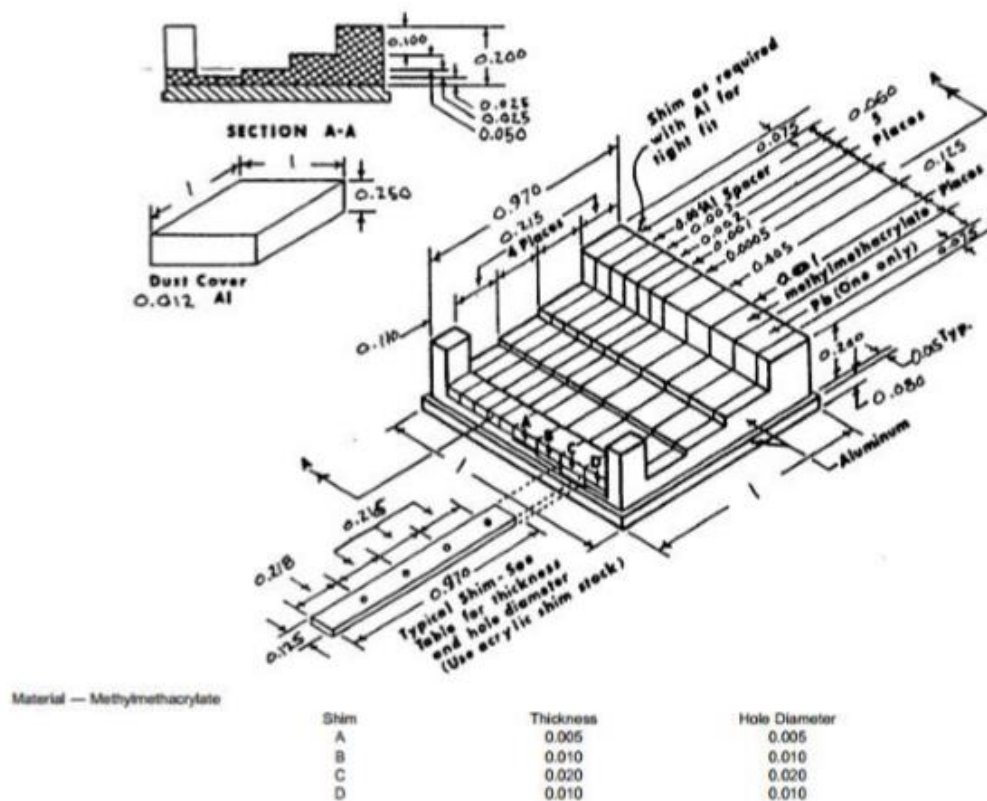


Figure 13 Schematic of Beam Purity Indicator.

Table 2 Quantitative definitions of Beam Purity Indicator.

Variable	Description
D_B	Film densities measured through the images of the boron nitride disks
D_L	Film Densities measured through the images of the lead disks
D_H	Film density measured at the center of the hole in the BPI
D_T	Film density measured through the image of the polytetrafluoroethylene
ΔD_L	Difference between the two D_L values
ΔD_B	Difference between the two D_B values

The second indicator used is the Sensitivity Indicator (SI). This indicator qualitatively determines the sensitivity of the neutron radiograph by observing holes and gaps of known dimensions between each shim. The SI schematic is shown in Figure 14.



The Effective Thermal Neutron content

$$NC = \frac{D_H - (higher D_B + \Delta D_L)}{D_H} * 100 \quad (11)$$

The effective Scattered Neutron Content

$$S = \frac{\Delta D_B}{D_H} * 100 \quad (12)$$

The effective Gamma Content

$$\gamma = \left(\frac{D_T - lower D_L}{D_H} \right) * 100 \quad (13)$$

The effective Pair Production content

$$P = \left(\frac{\Delta D_L}{D_H} \right) * 100 \quad (14)$$

From the radiograph of the SI, Figure 15 and Tables 4 and 5 were used to determine the value of G and H in Table 3.

The value of H is determined to be the largest consecutive numbered hole that is visible in the radiograph. The Value of G is determined to be the smallest gap that can still be seen in between the shims as shown in Figure 15.

Table 3 Neutron Radiography standards

Category	NC	H	G	S	γ	P
I	65	6	6	5	3	3
II	60	6	6	6	4	4
III	55	5	5	7	5	5
IV	50	4	5	8	6	6
V	45	3	5	9	7	7

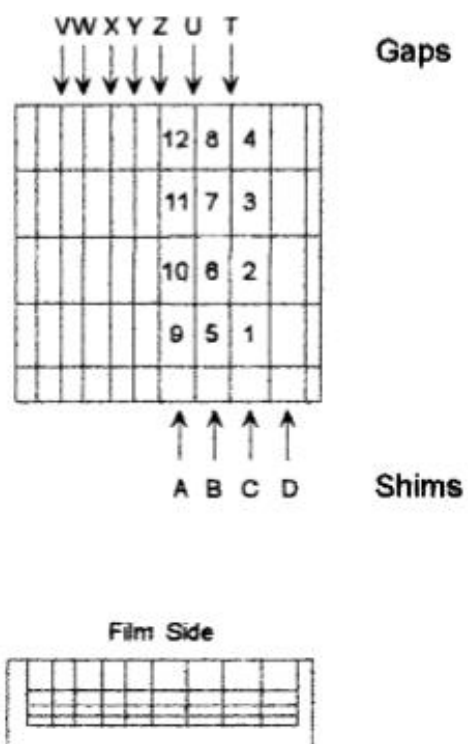


Figure 15 Sensitivity Indicator [28]

Table 4 Determination of H

Value of H	Shim
1	C
2	C
3	C
4	C
5	B
6	B
7	B
8	B
9	A
10	A
11	A
12	A

Table 5 Determination of G

Value of G	Gap
1	t
2	u
3	v
4	w
5	x
6	y
7	z

Optimally, the BPI and SI should be placed next together and taken in the same image. However, due to the incident viewing area of the detector, the BPI and SI had to be taken in separate images. Both the BPI and SI images were taken over a 4-minute exposure time at 10% reactor power.

2.5 Cadmium Strip

A cadmium strip provided by Nova Scientific was imaged to obtain additional data on the detectors image resolution and sharpness. Illustrated in Figure 16, the strip was a 0.050 cm thick cadmium strip with a series of holes along the center line. The holes ranging from sizes from 250 to 2150 μm with the smallest separation between holes measuring at 250 μm . The strip was exposed to the thermal neutron flux for 8 minutes at 10 % power.

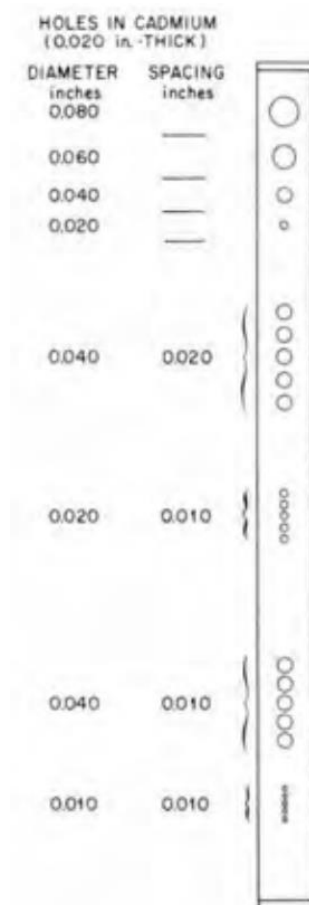


Figure 16 Schematic of Cadmium strip in inches

2.6 Beam Evaluation Throughout a Day

A test was performed to determine if the neutron flux and gamma concentration change throughout an entire day of reactor operations. This was performed by placing an ion chamber in front of the detector in line with the collimator. Using the ion chamber to calculated the exposure to air from gamma and the MCP detector to measure neutrons per second. A measurement was taken at various times of the day to evaluate if the detector saw a difference in neutron flux while a second measurement was made to determine if there was a change in gamma flux. Prior to startup, initial measurements were taken with

the shutter closed and open to get an initial level of flux and exposure. Measurements were also taken at 15 W, which is the lowest power level the reactor is typically run at. Counts per second were successfully recorded by the detector at every hour including post startup.

Once initial set up and baseline determinations were completed, a measurement was taken once the reactor reached full power (1MW) with the shutter open. After the first measurement, all measurements were taken at the top of every hour through the working day. Once the reactor was shut down, measurements were taken with the shutter still open at 5, 15 and 30 minutes after shut down. Measurements can be seen in Table 9 and Table 10.

2.7 Reactor Power Evaluation

A test was performed to evaluate the count rate and coincidence at different reactor power levels to determine the optimum operating voltage for the detector at various reactor power levels. This test was done because at 1MW (100% reactor power), the detector was being overloaded with neutron and was unable to get adequate contrast in projections taken. Measurements were taken at reactor power levels of 10%, 30%, 50%, 70%, 90%, and then once more at 10% of full power. At each power level, the counts per second successfully recorded by the detector were measured at various applied voltages. These voltages were measured at 50V increments from 3400V to 3900V.

The coincidence rate is the percentage neutrons that interact with the MCP and are recorded by the detector. [29]. At various voltages, the coincidence was also recorded to show the various delay line detection (DLD) events that passed the FPGA filter elements. According to NOVA, the coincidence upon the detector should be near 80% to ensure the detector is successfully recording events for an adequate signal-to-noise ratio. The

coincidence is directly related to the detector efficiency. As the coincidence of events within the detector increases so does the detector efficiency.

2.8 Radiography Reconstruction

Radiographs are essentially interpretations of the loss of neutrons from the beam due to absorption or scatter in an object of interest. This manifests itself as a measure of the change of intensity throughout the image due to the object attenuating the beam prior to hitting the detector.

After each image, post-radiograph processing was required. For optimum sharpness and/or contrast post-processing is done to clean up each image. Issues that can reduce the quality of the image include noise from the detector, foreign objects in the field, ghosting, or non-uniform image collection.

Using the image processing software ImageJ, images were processed after each shot exposure. For most corrections, a background image, or flat field, is taken before each shot or group of shots for a desired object being imaged. The flat field is an image that is taken without the object of interest in the field of view. During post-processing the flat field is divided into the raw image containing the desired object to be viewed. This method of normalizing an image reducing the electronic noise and increasing the signal to noise ratio. The software uses the following equation to normalize the intensities across the image:

$$I_1 = \left(\frac{i_1}{i_2} \right) * k_1 + k_2 \quad (15)$$

where i_1 is the new 8-bit photo after processing, i_1 is the image with the desired object, i_2 is the background, k_1 is the average intensity in i_1 , and k_2 is a minimum intensity which was always 0.

Multiplying by the k_1 correct the shifting of the intensity histogram between high intensity pixel outliers throughout the radiograph. After this, the image may need to be further processed by adjusting the contrast or smooth/sharpen the image based on what is trying to be viewed. Figure 17 shows the process at which the radiographs are processed and corrected. The top images of Figure 17 show the flat field and BPI prior to image corrections. Using equation 13, the flat field (Figure 17a) image was removed from the original BPI image, resulting in the bottom left image of Figure 17. The result of this image show the removal of detector noise. The image was then processed by enhancing contrast, which yields the final image for the BPI in the bottom right of Figure 17.

The final image allows for measurements to be more accurate and precise to determine specific conclusions on detector capabilities and standards.

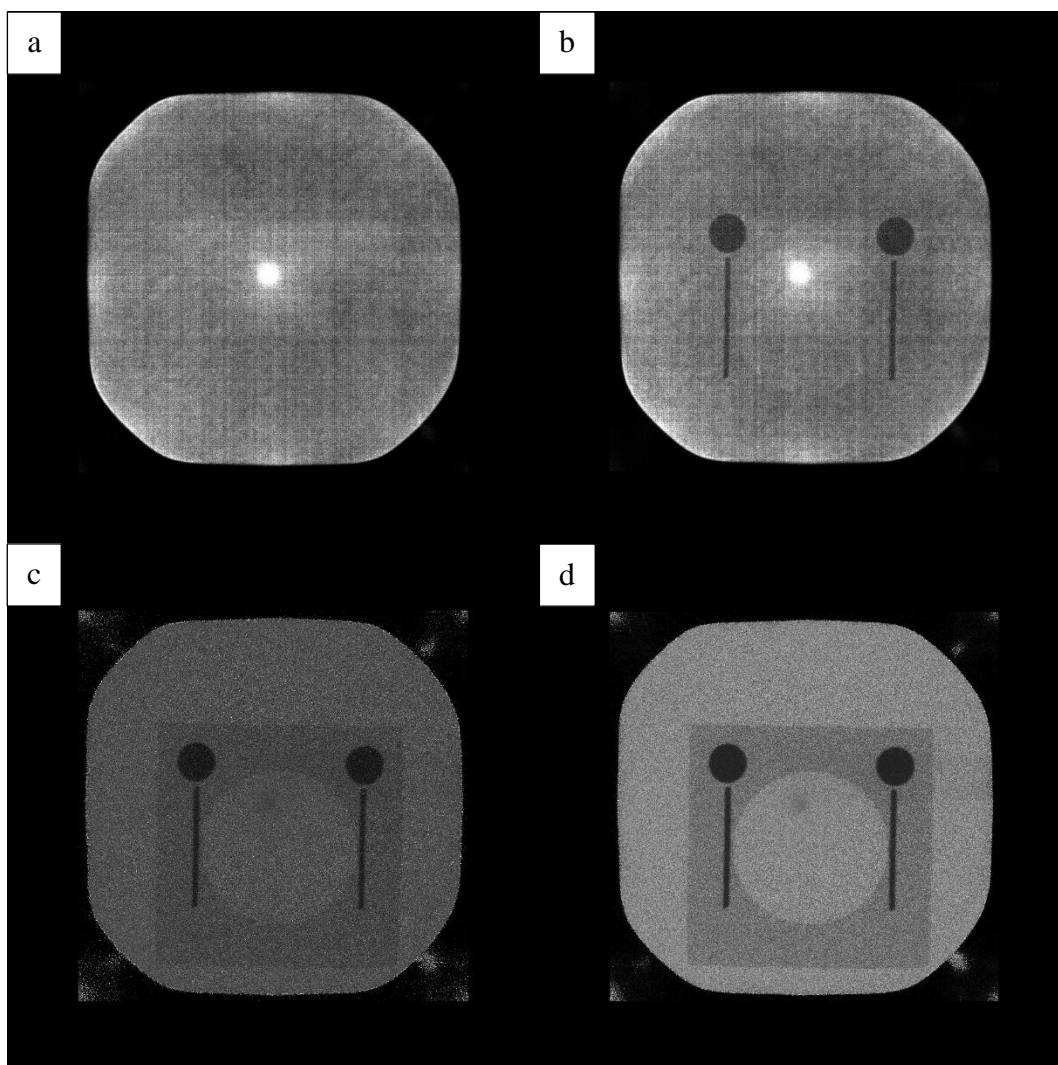


Figure 17 Various images and results of post imaging processing. In the top left (a) is an image of the flat field. Top right (b) is an image of the BPI. Bottom left (c) is an image of filtered BPI. Bottom right (d) is an image of the Final image with enhanced contrast.

2.9 Tomography Reconstruction

For tomography reconstruction, post-processing is similar to radiography reconstruction, but the process is applied to multiple images of an object rotated about a common axis. This was done by placing the desired object on a motorized stage to precisely rotate the object. A 500mm linear travel (IMS500PP) and 360-degree rotational (URS75BPP) stage were acquired from the Newport Corporation. Newport's in house

software allows stages to be controlled remotely from outside the NRF as seen in Figure 18 through 20.

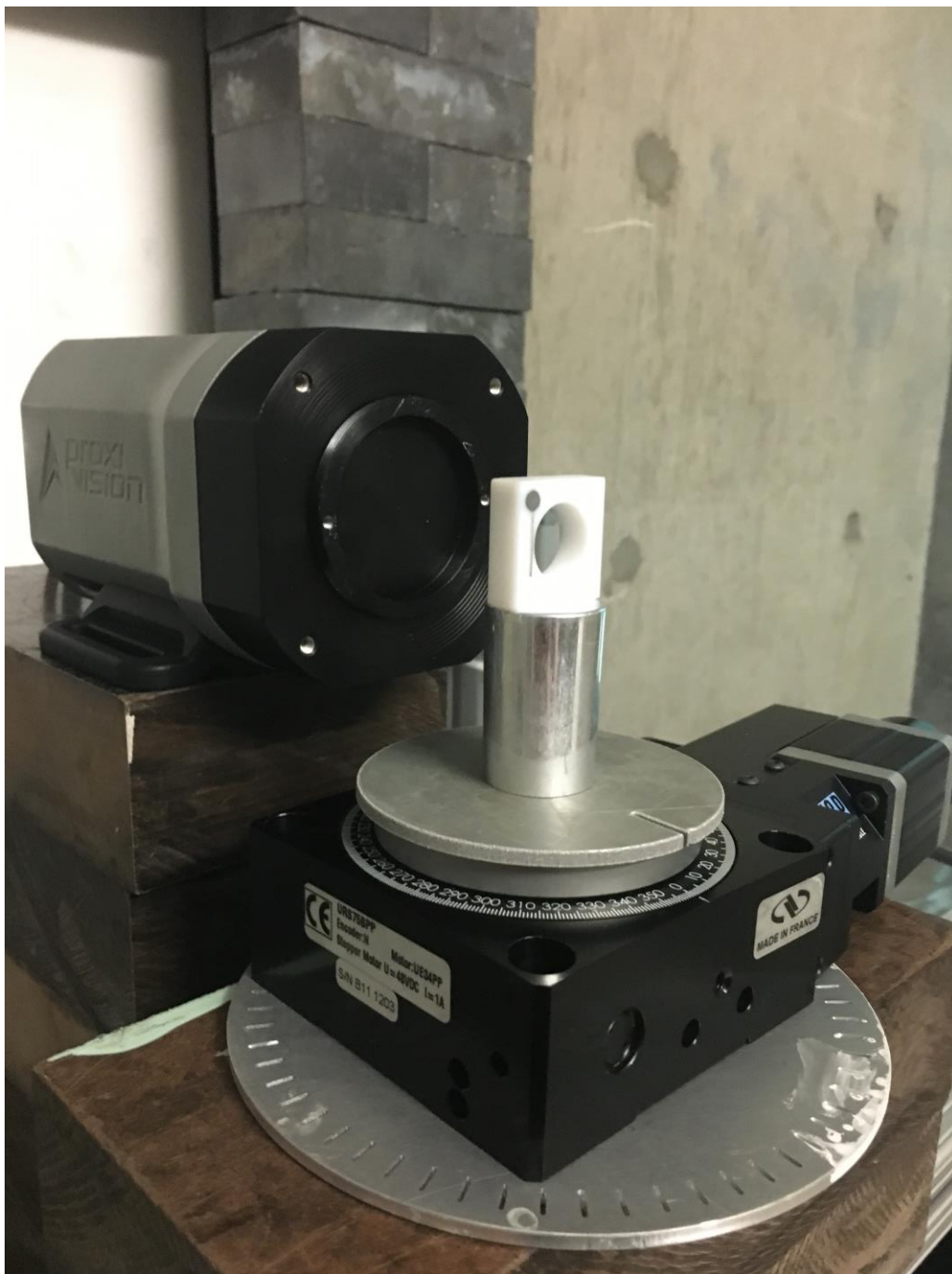


Figure 18 Detector setup with BPI



Figure 19 Overall set up for tomography of BPI including linear and rotational stages.



Figure 20 Motion controller used for motorized stages

This allows the desired object to be moved horizontally and rotated about the z-axis while keeping the shutter for the beam open. For adequate tomography, radiography images need to be taken through a minimum of 180° . This is required when trying to

visualize internal structures of an object with-out the superposition of over-and under-lying structures.

Recorded images are reconstructed in to sinograms. A sinogram is a 2D image in which the horizontal axis represents the count location on the detector while the vertical axis represents the angular position of the detector with respect to the object. [30] These images are mapped together in to a row and plotted where each image represents a measurement at angle, Θ , and plotted as a function of the pixel number. As the number of images taken around the object are increased, the number of possible solutions is reduced.

The next step at building the 3D model is the reconstruction process. To construct an adequate tomography, enough radiographs have to be taken to cover 180 (degree) of the object. Below is an example of the Algebraic Reconstruction Technique (ART) or referred to as the Kaczmarz's algorithm in linear algebra. It is an iterative class algorithm. This algorithm is given by the equation:

$$f_j^{(k+1)} = f_j^{(k)} + \frac{g_j - \sum_{j=1}^N f_{jt}^{(k)}}{N} \quad (16)$$

where $f_j^{(k)}$ and $f_j^{(k+1)}$ are the current and new pixel estimations, N the number of pixels along a ray; $\sum_{j=1}^N f_{jt}^{(k)}$ is the sum of radioactive counts in the N pixels for the k^{th} iteration; g_j is the measured number of counts for ray j. [30] This process is illustrated in Figure 21 for a four-pixel example.

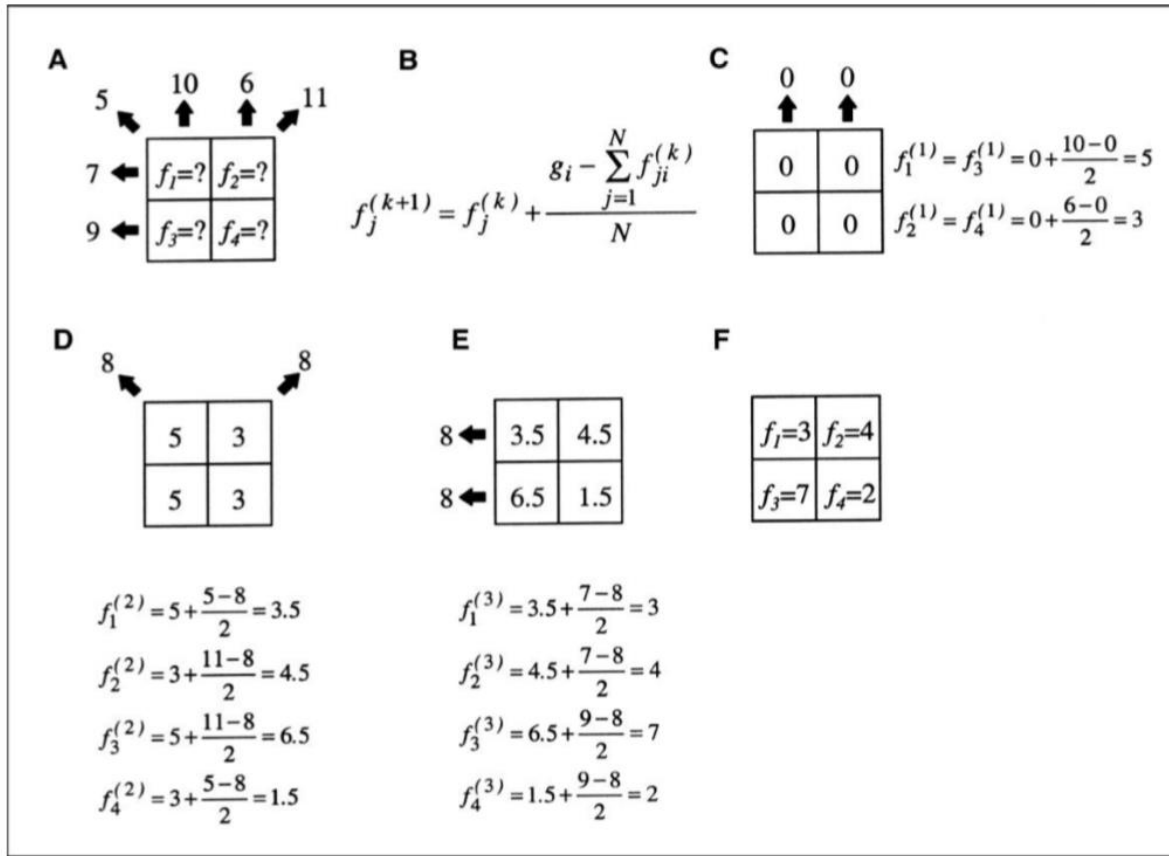


Figure 21 four-pixel example of the ART algorithm [30]

Beginning from the top left of Figure 21, Part A, the algorithm begins by finding values for the 4 pixels given the values in the 6 adjacent bins. In Part B, the Difference between the measured values and guessed values is determined and divided by the number of pixels in the given direction. From there the result is added to the current estimated value. In Part C, first inputs the estimated value in the vertical direction, then the algorithm updates the pixel values. The same method is applied for Parts D and E but in the oblique and horizontal vectors, respectively. Part F, shows the result of one full iteration of the ART algorithm.

When dealing with hundreds of rows and images, the algorithm shows the simplistic analogy of how the filtered back projection algorithm works within the software,

ImageJ. The filtered back projection algorithm assumes that each individual image represents a single measurement.

Using the BPI standard as the chosen sample for tomography, 2-minute exposures were taken every 1° about the z-axis. A flat field image was taken prior to every BPI exposure. ImageJ was then used to process the images.

A macro was written in ImageJ to process the images automatically, going through to remove flat field and enhance contrast for every image. The macro then arranged the images in order and placed them in a folder for stack rendering. After processing projections through ImageJ, Octopus Reconstruction software was used to render tomographic images [31].

Octopus is an image reconstruction software with the single purpose of rendering 3D volumes from 2D projections. The software is built with reconstructive functions for parallel, cone, fan, or helical cone beam setups.

Using Octopus Reconstruction Software, the processed images from ImageJ were first cropped to eliminate edge of scintillator to just the field of view. A cone beam setup was used within Octopus. By setting the source object distance and source detector distance very far away, the physics become similar to a parallel beam. The software was capable of adjusting and adjusting filter options to remove more noise from each projection. Once the projections were filtered, sinograms were rendered with the software. From back projection reconstruction, the sinograms are generated to represent each voxel as the image is rotated about the z-axis.

2.10 Concrete Samples

Supplied by the School of Construction Engineering Management and Civil Engineering, concrete samples were made for the purpose of quantifying water transportation through cement based mortar. This is a useful method to determine the degree of saturation within the entrained air cement. With each mortar sample made of a known volume of aggregate, water to cement ratio, and degree of hydration a degree of saturation for each sample can be determined.

There were four samples of different mix design: M3 Dry, M6 Dry, M3 Saturated, and M6 Saturated. Each Sample is shown in Figure 22 and have dimensions of 40mm x 75mm x 10mm.



Figure 22 Images of Entrained Air Cement based mortar samples: (Top Left) M3 Dry, (Top Right) M3 Saturated, (Bottom Left) M6 Dry, (Bottom Right) M6 Saturated

Just as with the IQI, before any radiographs of the samples were taken, a background image was taken without a sample present. This image again will be used to normalize the images of the samples removing noise. For the dry samples, radiographs were taken with an irradiation time of 10 min with the reactor power of 200 kW. Unlike with the IQI which was taken at 100 kW, the slight increase in power was to ensure enough neutrons attenuate through the concrete in a reasonable amount of time. After an image of the dry samples were taken, the samples were placed in water for 10 min to allow water to absorb up in to the mortar. Samples were then radiographed. After post processing, images with water and without water were compared.

3 Results and Discussion

3.1 Gold Foil Experiment

Table 6 shows values used to calculate the thermal neutron flux of beam port 3. It was determined that the thermal neutron flux at 1 MW was $9.42 \times 10^5 \pm 1.55 \times 10^4 \text{ n/cm}^2 \cdot \text{s}$.

Table 6 Measurements used for Gold foil experiment

Variable	Value
Irradiation Time (hr)	6.96
$\lambda_{\text{Au-198}}$ (hr^{-1})	6.17
$N_{\text{Au-197}}$ Bare Gold (atoms)	2.65×10^{20}
$N_{\text{Au-197}}$ Cd-Covered (atoms)	2.63×10^{20}
Thermal Cross Section (cm^2)	9.87×10^{-23}
Epithermal Cross Section (cm^2)	1.55×10^{-21}
Activity Bare (Bq)	3.17×10^3
Error of Activity Bare (Bq)	5.20×10^1
Activity Cd-Covered (Bq)	9.34×10^2
Error of Activity Cd-Covered (Bq)	1.53×10^1

3.2 Detector Efficiency

To calculate the product of P1 and P2, the rate of neutrons incident on the detector and the number of neutrons registered must be calculated. Knowing the neutron flux, the number of neutrons incident on the detector can be calculated by:

$$9.42E5 \frac{\text{neutrons}}{\text{cm}^2\text{s}} * \pi * (2\text{cm})^2 = 1.184E7 \frac{\text{neutrons}}{\text{s}} \quad (9)$$

The number of neutrons registered was calculated from the detector software during exposure, which was approximately $6.5E5 \text{ neutrons s}^{-1}$. The total efficiency, Q_n , was calculated to be;

$$Q_n = P_1 * P_2 * P_3 = \frac{6.5E5 \frac{\text{neutrons}}{\text{s}}}{9.42E5 \frac{\text{neutrons}}{\text{s}} * \pi * (2\text{cm})^2} * 100 = 5.49\% \quad (10)$$

3.3 Standards

For the standards to be evaluated, a flat field image was taken before each image of the SI and BPI to remove noise. Figure 23 shows the resultant images of the SI and BPI that were used for characterization of the beam and detection system.

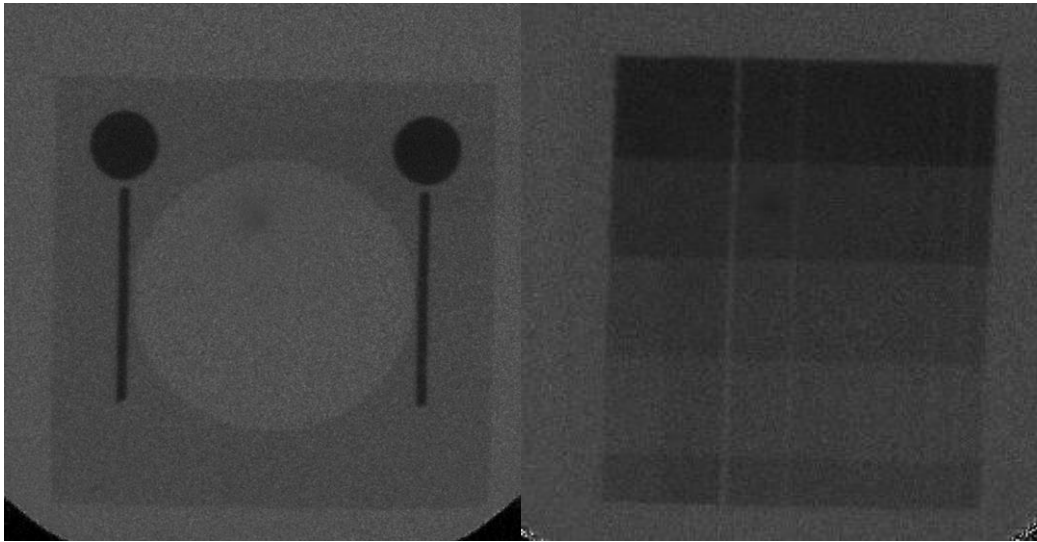


Figure 23 BPI (left) and SI (right) used for beam quality evaluation.

Using Table 3, the category for the detector system was determined. The results from the standards evaluation using the IQI system from ASTM 545 suggest that the system falls into a Category 3 radiography system, with results varying from a Category I to Category V. These measurements are shown in Table 7.

Table 7 International ASTM E545 suggested values for NDDL 40 Detector

Variable	NC	H	G	S	γ	P
Value	65	3	5	5	3	3
Category	I	V	V	I	I	I

3.4 Cadmium Strip

The spatial resolution of the detection system was found to be in the range of 50 to 200 μm . With respect to imaging, resolution is defined as the smallest known measurement that is discernible. The measurements were accurately determined through image processing to correct any distortions, noise and/or contrast alteration, and imaging objects of known dimensions. Contrast of images played a large significance in the result of final resolutions of many radiographs. Discerning Figure 24 shows the radiograph of the

cadmium strip used to help determine the spatial resolution. The Figure 24 has been marked to show the smallest holes in the strip measure at $200\text{ }\mu\text{m}$. These are the smallest holes in the strip of known dimension with a known spacing of $200\text{ }\mu\text{m}$ between each centerline.

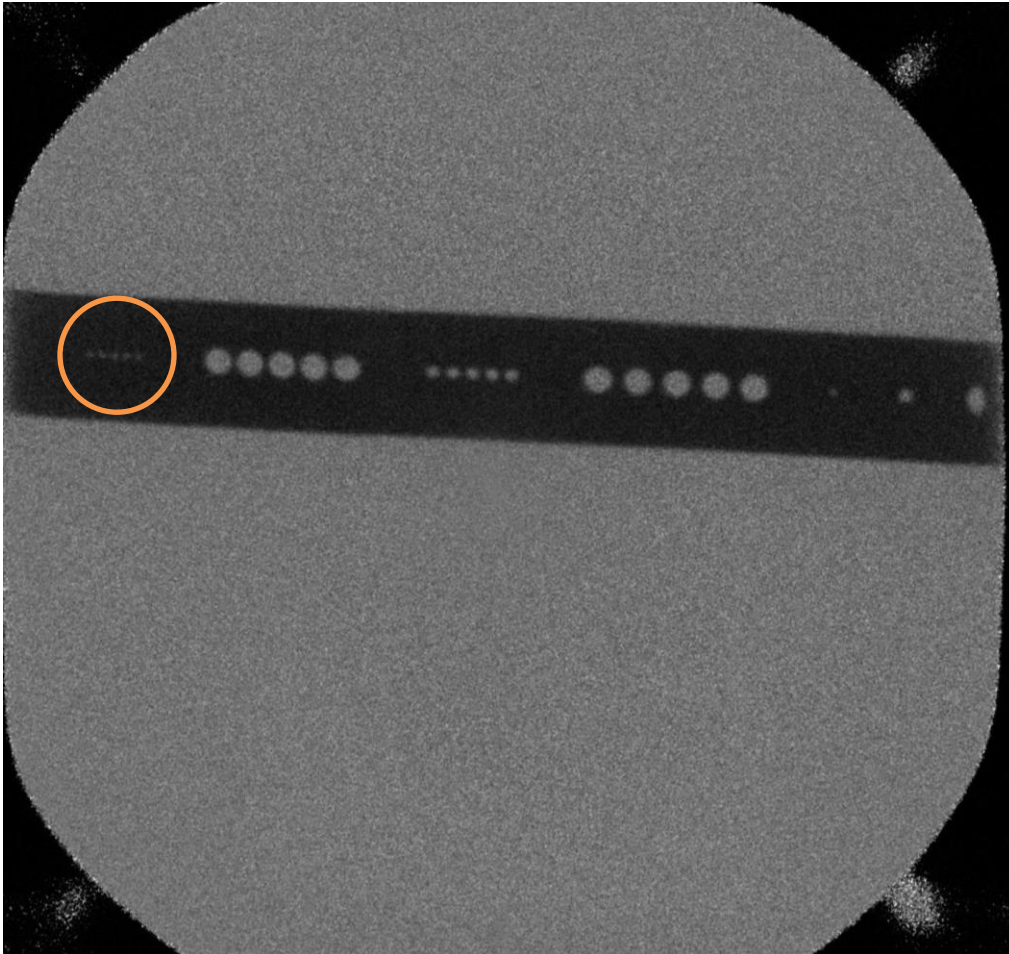


Figure 24 Image of Cadmium Strip with various tolerances.

3.5 Beam Evaluation Throughout a Day

Table 8 shows measurement taken prior to start up. Table 9 shows the results measured at the top of every hour. It is shown that throughout the day gamma exposure is constant at 3 R/hr at full reactor power. Table 10 shows the final measurements taken at

various times after shut down to show how fast the exposure drops off from what it was at full power.

As part of the investigation, NOVA Scientific suggested that poor contrast and signal to noise ratio of the detector were caused by high numbers of gamma interactions with the MCPs of the detector. So the test was performed to evaluate that gamma exposure throughout a day.

Table 8 Initial Measurements prior to test of measure the change in flux and exposure over a MW day.

Prior to Startup	Counts (n/sec)	Exposure (R/hr)
Shutter Closed	75	0
Shutter Open	125	0
15 Watts	-	-
Shutter Closed	75	0
Shutter open	200	0

Table 9 Results of Flux determination and gamma exposure

Time	Counts (n/sec)	Exposure (R/hr)
9:00	6.00E+05	3
10:00	6.00E+05	3
11:00	6.00E+05	3
12:00	6.00E+05	3
1:00	5.00E+05	3
2:00	4.00E+05	3
3:00	4.00E+05	3

Table 10 Measurements after shutdown.

Time (min)	Counts (n/sec)	Exposure (R/hr)
5	4000	0.2
15	1500	0.1
30	1500	0

3.6 Reactor Power Evaluation

Results of the reactor power evaluation experiment are shown in Table 11. At every percentage of reactor power, results show that there was an increase in detector coincidence with increase in voltage. This is better illustrated in Figure 25. The trend indicates a plateau at 3850V or higher.

Table 11 Results of measured counts at various voltages through different reactor power levels.

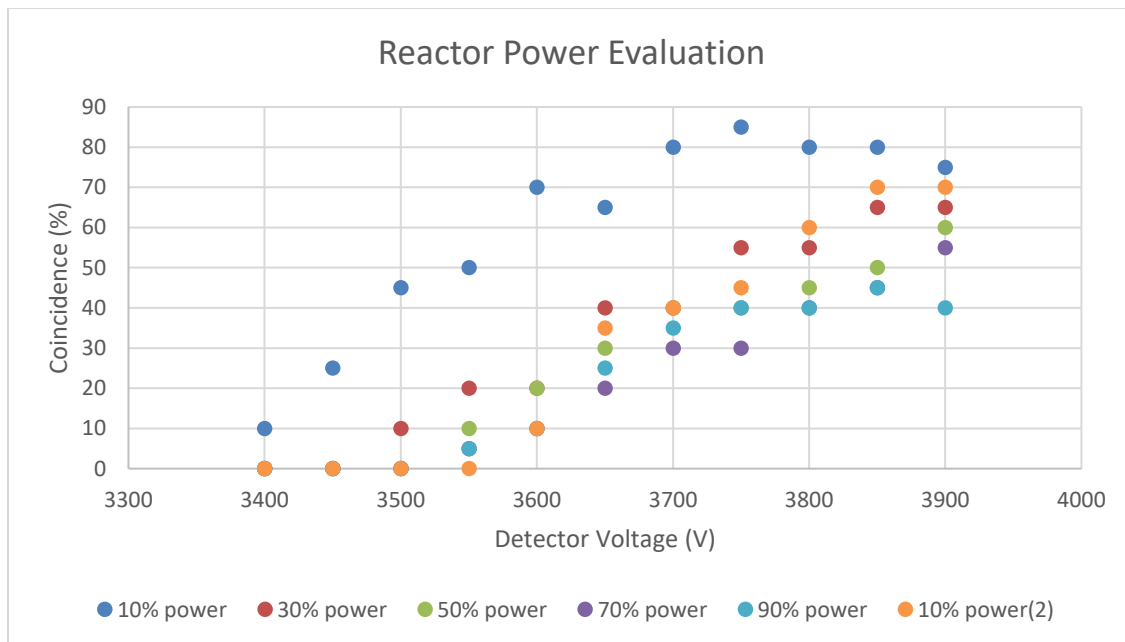
Reactor Power (% of 1MW)	Detector Voltage (V)	Detector Count Rate (cps)	Percent Coincidence (%)
10	3400	1.00E+04	10
	3450	3.50E+04	25
	3500	9.00E+04	45
	3550	1.50E+05	50
	3600	2.00E+05	70
	3650	3.00E+05	65
	3700	3.60E+05	80
	3750	4.10E+05	85
	3800	5.00E+05	80
	3850	6.00E+05	80
	3900	7.50E+05	75
30	3400	0	0
	3450	2.00E+02	0
	3500	2.50E+03	10
	3550	1.50E+04	20
	3600	7.00E+04	20
	3650	1.00E+05	40
	3700	2.50E+05	40
	3750	4.50E+05	55
	3800	6.50E+05	55
	3850	9.50E+05	65
	3900	1.20E+06	65
	3400	0	0
	3450	0	0
	3500	0	0
	3550	600	10
	3600	7500	20

Reactor Power (% of 1MW)	Detector Voltage (V)	Detector Count Rate (cps)	Percent Coincidence (%)
50	3650	3.50E+04	30
	3700	1.25E+05	40
	3750	3.00E+05	40
	3800	6.00E+05	45
	3850	9.00E+05	50
	3900	1.30E+06	60
70	3400	0	0
	3450	0	0
	3500	0	0
	3550	300	5
	3600	4500	10
	3650	2.50E+04	20
	3700	1.00E+05	30
	3750	2.50E+05	30
	3800	5.50E+05	40
	3850	9.00E+05	45
90	3900	1.25E+06	55
	3400	0	0
	3450	0	0
	3500	0	0
	3550	200	5
	3600	4500	10
	3650	2.50E+04	25
	3700	1.00E+05	35
	3750	2.00E+05	40
	3800	4.50E+05	40
	3850	7.50E+05	45
	3900	1.00E+06	40

Table 12 shows a series of measurement repeated at 10% reactor power. From the measurements, it was determined that the optimum voltage at which produced the best coincidence for operation of the detector was 3850v at 10% reactor power.

Table 12 The second set of measurements taken at 10% power

Reactor Power (% of 1MW)	Detector Voltage (V)	Detector Count Rate (cps)	Percent Coincidence (%)
10	3400	0	0
	3450	0	0
	3500	0	0
	3550	0	0
	3600	700	10
	3650	5500	35
	3700	25000	40
	3750	8.50E+04	45
	3800	1.75E+05	60
	3850	3.00E+05	70
	3900	4.30E+05	70

**Figure 25 Graph of coincidence vs detector voltage at various reactor power levels.**

3.7 Tomography

A completed tomographic image was produced using the Octopus imaging software. Figure 26 shows a pair of sinograms that were rendered using radiographs of the

BPI. Figure 26 (b) follows the boron sphere of the BPI while the sinogram on the right, Figure 26 (c), shows the path the cadmium wires within the BPI. It can also be seen in each sinogram that there are inconsistencies as the object travels. An example of inconsistent location is shown in Figure 26 (b). This is due to loss of contrast from a poor signal to noise ratio of the NDDL40 detector system.

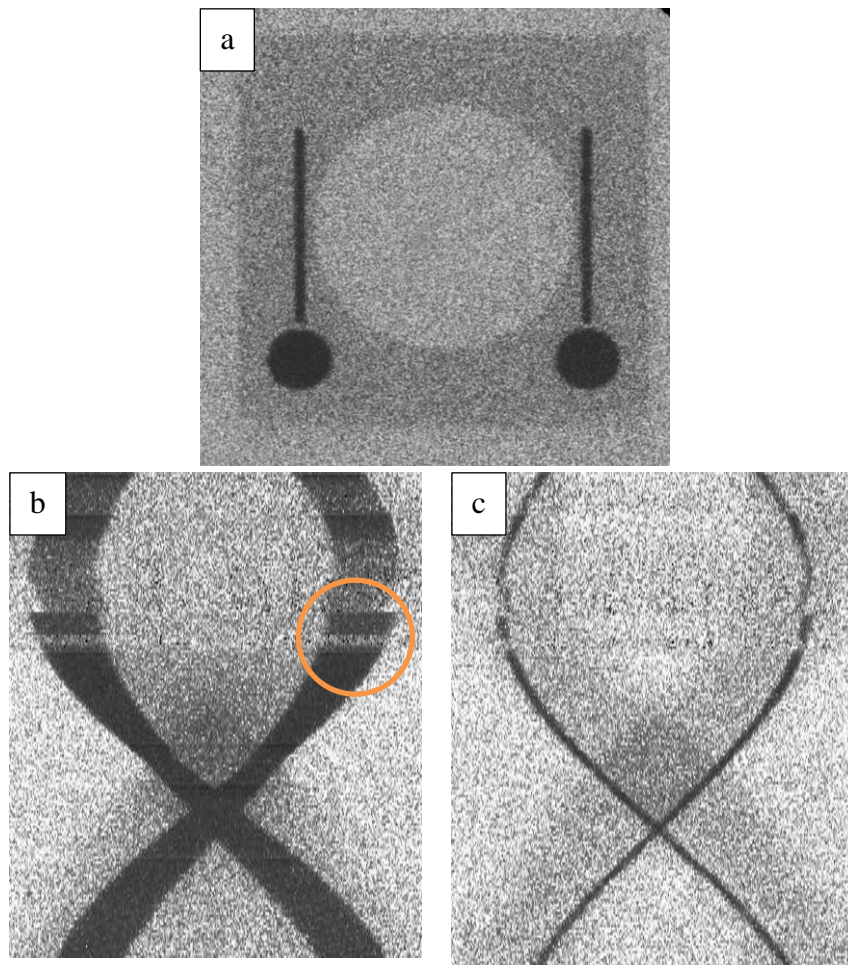


Figure 26 BPI and represented Sinograms.

In Figure 27 through Figure 30 below, examples of the tomographic model are shown.

Even though there were inconsistencies in the sinograms due to the poor image quality of

radiographs, the quality of the tomography rendering was adequate. There is a clear distinguishability between boron sphere and cadmium wire.

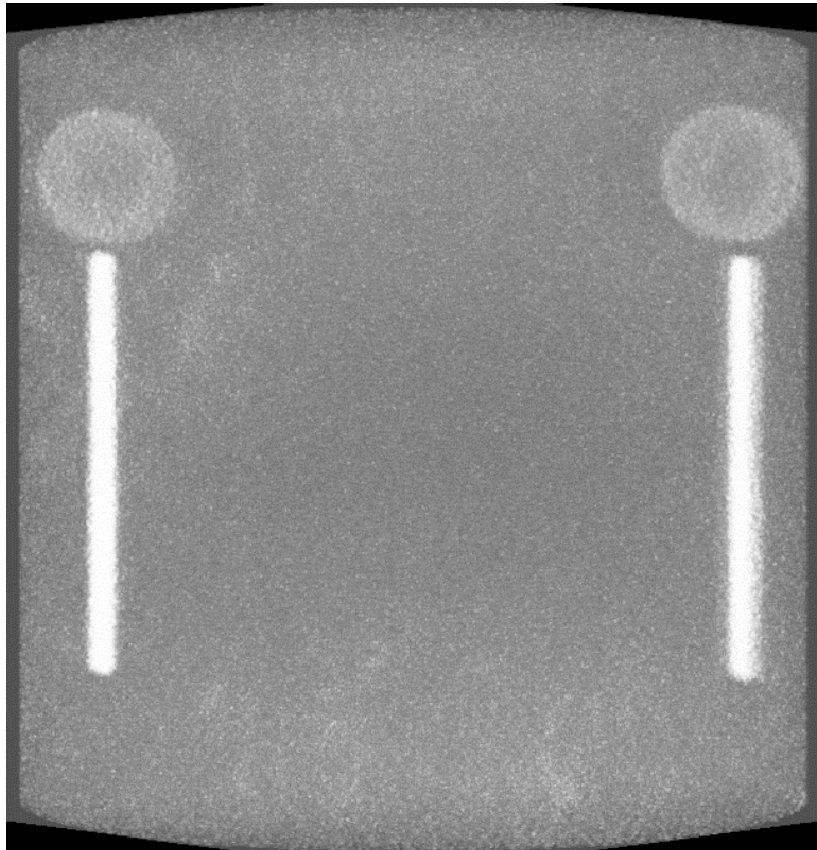


Figure 27 Front View of BPI Tomographic image



Figure 28 Side View of BPI Tomographic Image

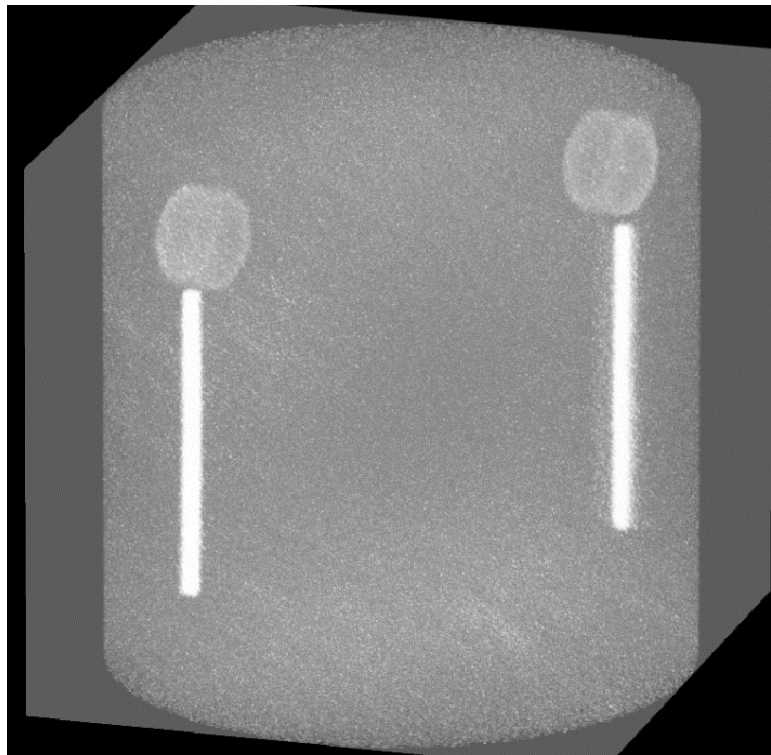


Figure 29 Isomeric view of BPI Tomographic image

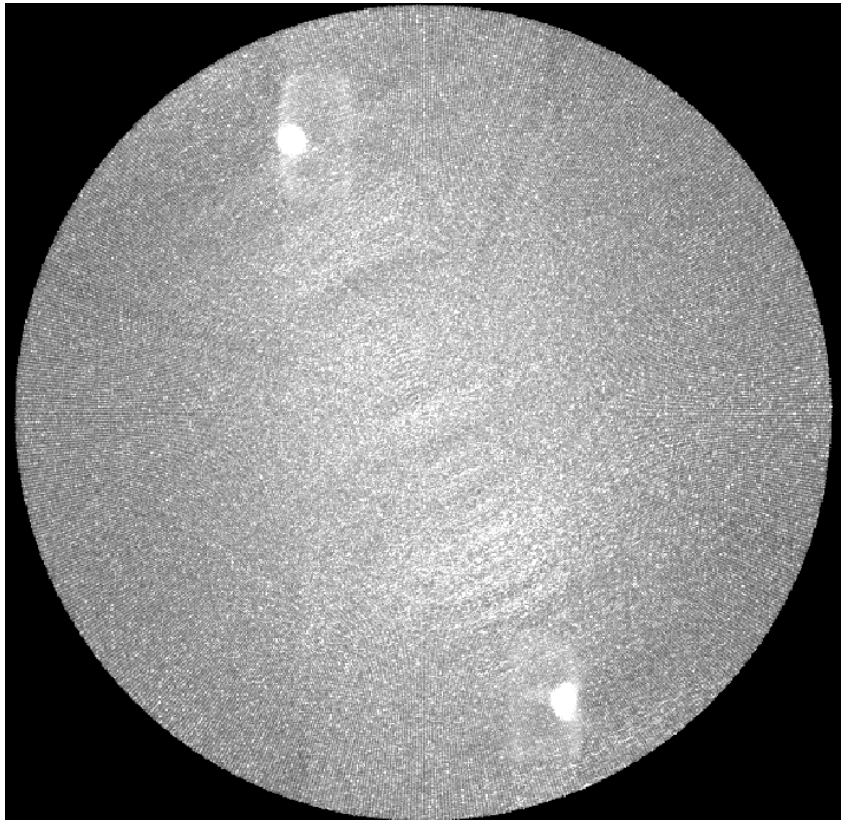


Figure 30 Top view of BPI Tomographic Image

3.8 Complications

Even though these images were taken using a digitally capable detector system, it is the instability of this detector making tomography impractical. Detector efficiency was decreased due to the dynamic background, detection coincidence, signal to noise ratio and inconsistencies of the detector system. For most of the research, the coincidence was never able to maintain higher than 50-60%. The low coincidence resulted in a poor signal to noise ratio which leads to radiographs having poor contrast.

Having to run the reactor at 10% power to get adequate results from detector was very inconvenient. Shown in Figure 31, images taken at a reactor power of 1 MW result in an inverted image and the contrast is poor.

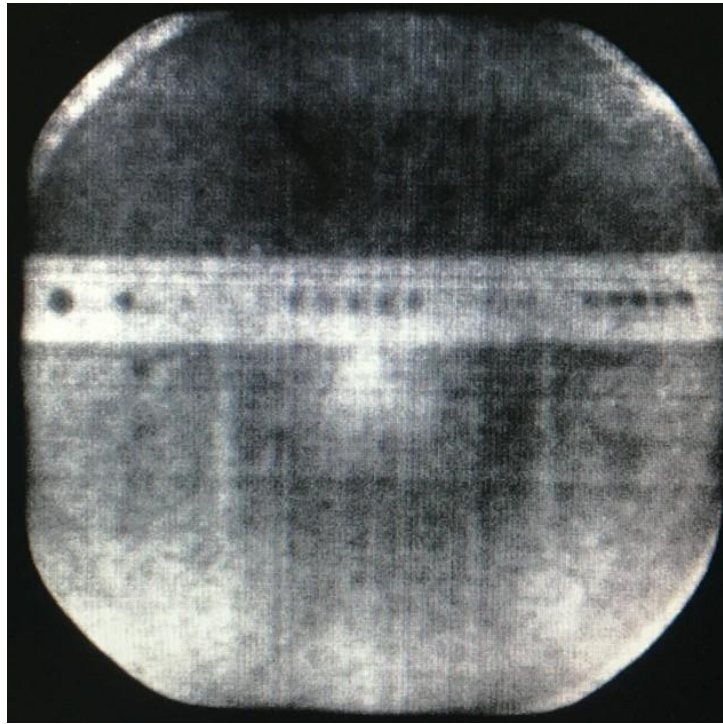


Figure 31 Image of cadmium strip at 100% reactor power.

Figure 31 should be showing attenuation of neutrons from the cadmium but it is actually showing the inverse. This is due to the neutron flux being too high for the detector, essentially over loading the MCP glass stack and anode wires. In turn this creates increased dead time in the detector system. This suggests that the anodes become over-saturated with electrons. The inversion is specifically due to the software reading these overloaded channels as zero on a gray scale readout. A solution initially was to moderate the beam with aluminum. The problem with this solution was that it would have required an aluminum filter with a thickness of 8 inches.. Lowering the reactor power (i.e. the thermal neutron flux) was found to yield the best results for taking radiographs using this detector.

Another significant issue with the detector system is the requirement of having to take a flat field prior to every radio graph. When a flat field was not taken prior to each

radiograph, a latent image would remain from the immediately previous radiograph. An example of this is shown in Figure 32. This “ghosting,” essentially prevents a tomographic model from being rendered.

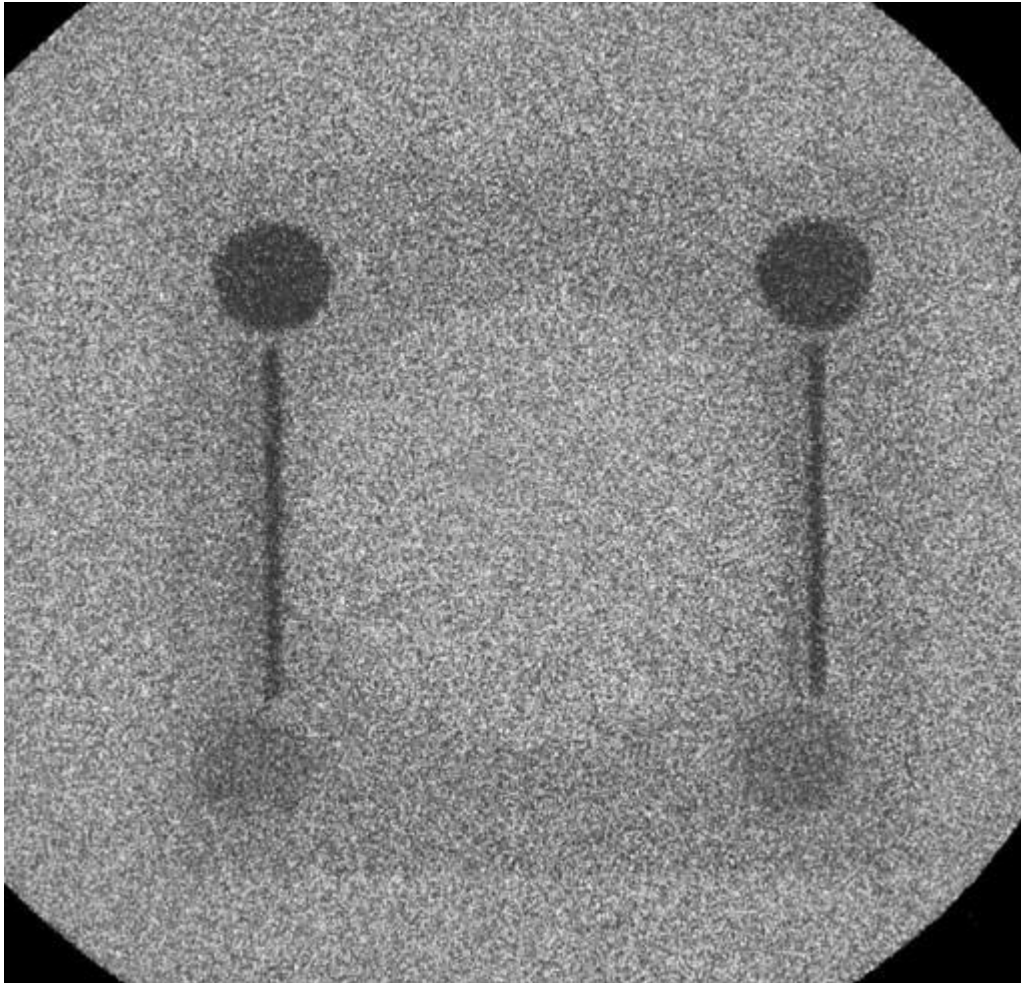


Figure 32 Example of an image taken with dual exposure.

Images taken by the NDDL40 detector continually decreased in contrast as a function of time. Initially the detector was operated at 3,450 V and required increasing to 3,850 V. Due to a loss of signal to noise ratio over time resulting in poor contrast of radiographs, the voltage had to be increased 3,950 V allowing for a higher coincidence upon the detector at 10% power. This issue is due to the anode not getting enough voltage

bias to completely sweep electrons from the anode. The higher voltage resulted in an increase in electronic noise from the detector. Most of this noise is removed or reduced by taking a background image for every image taken. Most of the noise is represented as a dot in the middle of radiographs, even after processing. White pixels represent saturated areas on a grey scale. A bright spot represents a lot of interactions from incoming neutrons upon the detector in that location. When there is artificial noise from the detector, it is registered as more neutrons. In raw images this is represented as a bright white spot in the center of the FOV as shown in Figure 33.

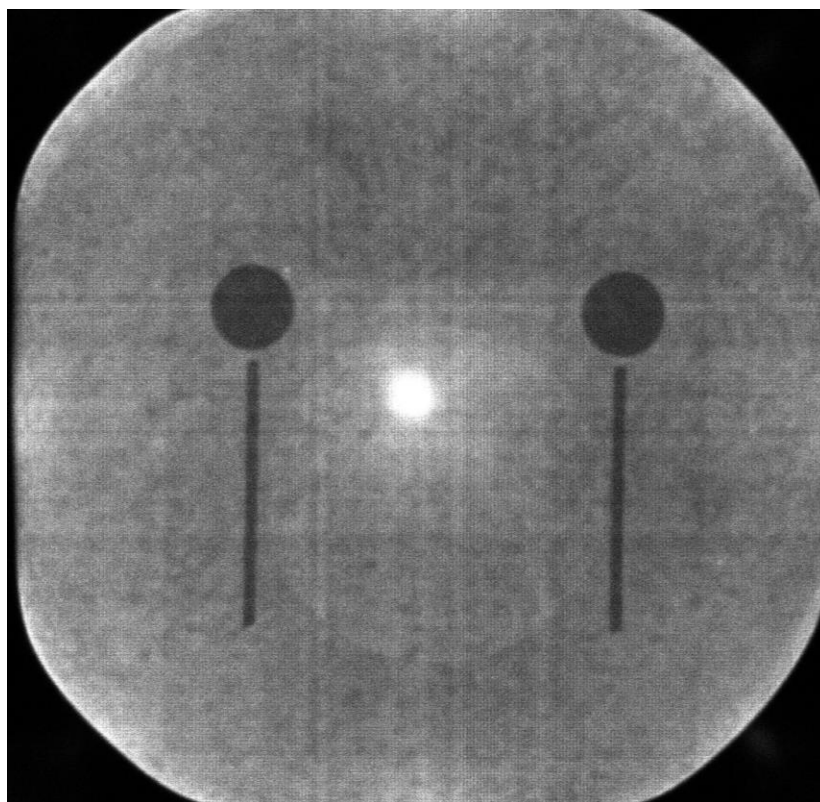


Figure 33 BPI image with electronic noise

4 Conclusion.

The objective of this work was to investigate efficiency and spatial resolution of the NDDL40 MCP vacuum sealed detector from NOVA Scientific for the use of neutron radiography and tomography. The detector is based on using borated micro channel glass plates to detect incoming thermal neutrons through the $^{10}\text{B}(\text{n},\alpha)^7\text{Li}$ interaction.

The NDDL 40 MCP detector has been shown to be capable of producing both radiographs and tomographic images but it is not practical nor useful. Radiographs continually had inconsistent results in image quality due to the dynamic background, signal-to-noise ratio and dramatic decrease in detector efficiency. This led to issues in the rendered tomographic models. In the end, more than half of the 190 images taken for tomography had to be retaken.

Through the process of measurements, methods of determination, and ASTM standards the NDDL-40 MCP detector was determined have to and optimum efficiency of 6% with a maximum spatial resolution of 50 to 200 μm .

5 Future Work

Future research with this detector will need to be done to determine solutions for the use of imaging concrete sample of evaluating water saturation levels over time. Concrete samples will be made and placed into one of two Relative Humidity and Temperature (RH/T) chambers purchased from Darwin Chambers Company. The First chamber is a cabinet style environmental chamber that will be used to store large amount of samples that will be used frequently and will be moved in and out of the chamber frequently for radiography. The second, but smaller chamber will be used for a few samples that will remain the chamber during the radiography examination. This is used so that the environmental variables remain constant.

A solution will need to be found for the degradation in contrast over time of the detector. This would reduce the number of images required for tomography and decrease the allotted time it takes to perform tomography. This would result in an increase in overall detector efficiency and overall tomography of reasonable quality.

Bibliography

- [1] H. Berger, Neutron Radiography Methods, Capabilities, and Applications, New York: Elsevier Publishing Company, 1965.
- [2] J. E. Turner, Atoms, Radiation, and Radiation Protection, Weinheim: WILEY-VCH Verlag GmbH & Co. , 2007.
- [3] M. R. Hawkesworth, "Radiography with Neutrons Conference, September 1973," London, 1975.
- [4] J. P. Barton, G. Farny, J.-L. Person and H. Rottger, "Neutron Radiography: Proceedings of the Second World Conference," Paris, 1987.
- [5] J. C. Domanus, Practical Neutron Radiography, Dordrecht: Kluwer Academic Publishers, 1992.
- [6] I. S. Anderson, R. L. McGreevy and H. Z. Bilheux, Neutron Imaging and Applications, New York: Springer Science, 2009.
- [7] D. S. Hussey, D. L. Jacobson, M. Arif, P. R. Huffman, R. E. Williams and J. C. Cook, New neutron imaging facility at the NIST, Gaithersburg, MD: Nuclear Instruments and Methods in Physics Research A 542 9-15, 2005.
- [8] A. Sinha, P. S. Sarkar and A. Kashyap, "Applications of digital imaging at BARC (India) using reactor and nonreactor sources," *IEEE Transactions on Nuclear Science*, 2005.
- [9] A. G. Filler, "The History, Development and Impact of Computed Imaging in Neurological Diagnosis and Neurosurgery: CT, MRI, and DTI," *Nature Precedings* , 2009.
- [10] J. s. Brenizer, "A Reiview of significant advances in neutron imaging from conception to the present.," *Physics Prcedia* , pp. 10-20, 2013.
- [11] W. J. Williams, Neutron Radiography and Tomography: Determining and Optimizing Resolution of Neutron Sensitive Multi Channel Plate Detectors, Corvallis, 2013.
- [12] A. S. Tremsin, B. W. Felle and G. R. Downing, "Efficiency optimization of microchannel plate (MCP) neutron imaging detectors. I. Square channels with 10B doping," *Nuclear Intstruments in Physics Research A* 539, pp. 278-311, 2005.
- [13] T. Gys, "Micro-channel plates and vacuum detectors," *Nuclear instruments and methods in physics research A*, pp. 254-260, 2014.
- [14] G. W. Fraser, "The gain, temporal resolution and magnetic field immunity of microchannel plates," *Nuclear Instruments and Methods in Physics Research Section A: Accelerators, Spectrometers, Detectors and Associated Equipment*, pp. 595-606, 1990.
- [15] M. Y. Barnakov and A. V. Mironovv, "Photocathode aging in MCP PMT," *Workshop on fast cherenkov dettectors - photo detection, DIRC design and DAQ*, 2011.

- [16] T. V. Anderson, B. Dodd, J. Ringle and S. Menn, *Oregon State TRIGA Reactor Training Manual*, Corvallis, OR: Oregon State University.
- [17] A. International, "Standard Test Method for Determining Image Quality in Direct Thermal Neutron Radiographic Examination.," pp. E545-05, 2010.
- [18] International Atomic Energy Agency, "Neutron Imaging: A Non-Destructive Tool for Material Testing," Vienna, 2006.
- [19] ASTM International, "Standard Test Method for Determining the L/D Ratio of Neutron Radiography Beams," Vols. E803-91, 2013.
- [20] S. Vaughn, "Investigation of a Passive, Temporal, Neutron Monitoring System that Functions Within the Confines of Start 1," 2003.
- [21] Brookhaven National Laboratory, "National Nuclear Data Center," 22 December 2011. [Online]. Available: <http://www.nndc.bnl.gov/exfor/endl00.jsp>.
- [22] S. Y. Chu, L. P. Ekstrom and R. B. Firestone, "WWW Table of Radioactive Isotopes," February 1999. [Online]. Available: <http://nucleardata.nuclear.lu.se/toi/nuclide.asp?iZA=790198>.
- [23] A. Konefal, "Undesirable Radioisotopes Induced by Therapeutic Beams from Medical Linear Accelerators," *Radioisotopes-Applications in Bio-medical Science*, pp. 127-150, 2014.
- [24] O. H. Siegmund, J. V. Vallerga, A. S. Tremsin, J. Mcphate and B. Feller, "High Spatial Resolution Neutron Sensing Microchannel Plate Detection," *Science Direct* vol. 576, pp. 178-182, 2007.
- [25] J. L. Wiza, "Microchannel Plate Detectors," *Nuclear Instruments and Methods Vol. 162*, pp. 587-601, 1979.
- [26] O. H. Siegmund, J. V. Vallerga, A. S. Tremsin, J. Mcphate and B. Feller, "High Spatial Resolution Neutron Sensing Minicochannel Plate Detectors," *Nuclear Instruments and Methods in Physics Research A*, pp. 178-182, 2007.
- [27] A. International, "Standard Practice for Fabrication of Neutron Radiographic sensitivity Indicators.," pp. Vol. 3.03. E2023-99, 2013.
- [28] International, ATSM, "Standard Test Method for Determining Image Quality in Direct Thermal Neutron Radiographic Examination.," pp. E545-05, 2010.
- [29] Surface Concept, *GUI DLD Software*, Mainz: Am Sagewerk 23a, 2012.
- [30] P. P. Bruyant, "Analytic and Iterative Reconstruction Algorithms in SPECT," *The Journal of Nuclear Medicine* , pp. 1343-1358, 2002.
- [31] Octopus Imaging, *Octopus Reconstruction User Manual*, Ghent, 2016.
- [32] C. L. Lucero, D. P. Bentz, D. S. Hussey, D. L. Jacobson and J. W. Weiss, "Using Neutron Radiography to Quantify Water Transportation and the Degree of Saturation in Entrained Air Cement Based Mortar," *10 World Conference on Neutron Radiography October 2014*, pp. 542-550, 2015.
- [33] E. M. Baum, M. C. Ernesti, H. D. Knox, T. R. Miller and A. M. Watson, *Nuclides and Isotopes Chart of the Nuclides*, seventeenth Edition, United States, 2009.

- [34] H. Cember and T. E. Johnson, Introduction to Health Physics, 4th Ed., McGraw-Hill Companies Inc., 2009.
- [35] N. Tsoulfanidis and S. Landsberger, Measurement and Detection of Radiation 3rd edition, Boca Raton: CRC Press, 2011.
- [36] A. M. Shaikh, "Development of neutron detectors and neutron radiography at Bhabha Atomic Research Centre," *Pramana journal of physics*, pp. 663-674, 2008.
- [37] I. W. Osborne-Lee and C. W. Alexander, "Californium-252: A remarkably Versatile Radioisotope," Oak Ridge National Lab, Oak Ridge, 1995.